nature biotechnology

Nanoscale imaging of clinical specimens using pathology-optimized expansion microscopy

Yongxin Zhao[1,11], Octavian Bucur[2–5,11], Humayun Irshad[2,3,5], Fei Chen[1,6,7], Astrid Weins[8,9], Andreea L Stancu[2,5], Eun-Young Oh[2], Marcello DiStasio[2], Vanda Torous[2], Benjamin Glass[2], Isaac E Stillman[2], Stuart J Schnitt[2], Andrew H Beck[2,3,5] & Edward S Boyden[1,6,7,10]

Expansion microscopy (ExM), a method for improving the resolution of light microscopy by physically expanding a specimen, has not been applied to clinical tissue samples. Here we report a clinically optimized form of ExM that supports nanoscale imaging of human tissue specimens that have been fixed with formalin, embedded in paraffin, stained with hematoxylin and eosin, and/or fresh frozen. The method, which we call expansion pathology (ExPath), converts clinical samples into an ExM-compatible state, then applies an ExM protocol with protein anchoring and mechanical homogenization steps optimized for clinical samples. ExPath enables ~70-nm-resolution imaging of diverse biomolecules in intact tissues using conventional diffraction-limited microscopes and standard antibody and fluorescent DNA *in situ* hybridization reagents. We use ExPath for optical diagnosis of kidney minimal-change disease, a process that previously required electron microscopy, and we demonstrate high-fidelity computational discrimination between early breast neoplastic lesions for which pathologists often disagree in classification. ExPath may enable the routine use of nanoscale imaging in pathology and clinical research.

Physicians and researchers have long examined cellular structures and molecular composition using diffraction-limited microscopy to diagnose or investigate the pathogenesis of a wide variety of predisease and disease states. Biomolecules themselves, however, are nanoscale in dimension and configured with nanoscale precision throughout cells and tissues. This organization has begun to be explored in basic science using pioneering super-resolution microscopy methods[1–4] as well as electron microscopy (EM)[5–7]; but such methods require complex hardware, can present a steep learning curve and are difficult to apply to large-scale human tissues. Accordingly, super-resolution imaging and nanoscopy have not found routine utility in clinical practice and are rarely applied to clinical samples, even in a research context.

Recently, we developed a strategy for imaging large-scale cell and tissue samples by physically, rather than optically, magnifying them[8]. In this strategy, ExM, we isotropically expand tissues by embedding them in a dense swellable polymer (e.g., a mesh of sodium polyacrylate synthesized evenly throughout a tissue) that binds key biomolecules or fluorescent labels to the polymer network. Samples are then mechanically homogenized and swelled, so that they can be imaged with nanoscale (~70 nm) resolution on conventional diffraction-limited microscopes. Although the original version of ExM required synthesis of a linker to couple fluorescent labels to the polymer, we recently developed protein retention ExM (proExM), a version of ExM that uses a commercially available anchoring molecule to tie proteins (such as fluorophore-bearing antibodies) directly to the swellable polymer[9].

Here, we report a clinically optimized form of proExM, ExPath, which can process most types of clinical samples currently used in pathology, including formalin-fixed paraffin-embedded (FFPE), hematoxylin and eosin (H&E)-stained and fresh-frozen human tissue specimens on glass slides. We explore ExPath's ability to enable nanoscale imaging on a wide variety of tissue samples from different human organs and disease states. In a small-scale study, we show that diseases (such as kidney minimal change disease (MCD)[10]) that previously required EM for diagnosis can now be directly and accurately diagnosed with ExPath and conventional diffraction-limited light microscopy. As another example, we used ExPath to analyze nuclear atypia of early breast neoplastic lesions for which pathologists often disagree in classification[11], and we show that ExPath facilitates computational pathology differentiation of hard-to-diagnose subtypes of these lesions. We anticipate that ExPath will have broad utility in enabling probing of nanoscale features at the genomic, protein and cell-morphology levels. ExPath will enhance the diagnostic power available to pathologists without requiring investment in novel hardware. We also expect the method will be useful for providing insights into the pathogenesis of various human diseases.

[1]MIT Media Lab, Massachusetts Institute of Technology, Cambridge, Massachusetts, USA. [2]Department of Pathology and Cancer Research Institute, Beth Israel Deaconess Medical Center, Harvard Medical School, Boston, Massachusetts, USA. [3]Ludwig Center at Harvard Medical School, Boston, Massachusetts, USA. [4]Institute of Biochemistry of the Romanian Academy, Bucharest, Romania. [5]Broad Institute of MIT and Harvard, Cambridge, Massachusetts, USA. [6]Department of Biological Engineering, Massachusetts Institute of Technology, Cambridge, Massachusetts, USA. [7]McGovern Institute, Massachusetts Institute of Technology, Cambridge, Massachusetts, USA. [8]Department of Pathology, Brigham and Women's Hospital, Harvard Medical School, Boston, Massachusetts, USA. [9]Department of Medicine, Renal Division, Brigham and Women's Hospital, Harvard Medical School, Boston, Massachusetts, USA. [10]Department of Brain and Cognitive Sciences, Massachusetts Institute of Technology, Cambridge, Massachusetts, USA. [11]These authors corresponded equally to this work. Correspondence should be addressed to A.H.B. (Andy.Beck@PathAI.com, pathological aspects) or E.S.B. (esb@media.mit.edu, technical aspects).

Received 29 June 2016; accepted 28 April 2017; published online 17 July 2017; doi:10.1038/nbt.3892

RESULTS

Clinical samples and pathology-optimized expansion microscopy

We first devised a series of steps to convert clinical samples to a state optimized for ExM processing (**Fig. 1** and **Supplementary Fig. 1**). We considered three starting tissue states—FFPE, H&E stained and fresh frozen; we assumed the tissue to be thin sliced and on a glass slide. We first investigated FFPE samples, since we hypothesized that the steps (e.g., xylene treatment, rehydration and antigen retrieval) required for converting tissues in the other categories would be subsets or permutations of the steps required for FFPE tissue processing. We evaluated whether xylene treatment to remove paraffin, followed

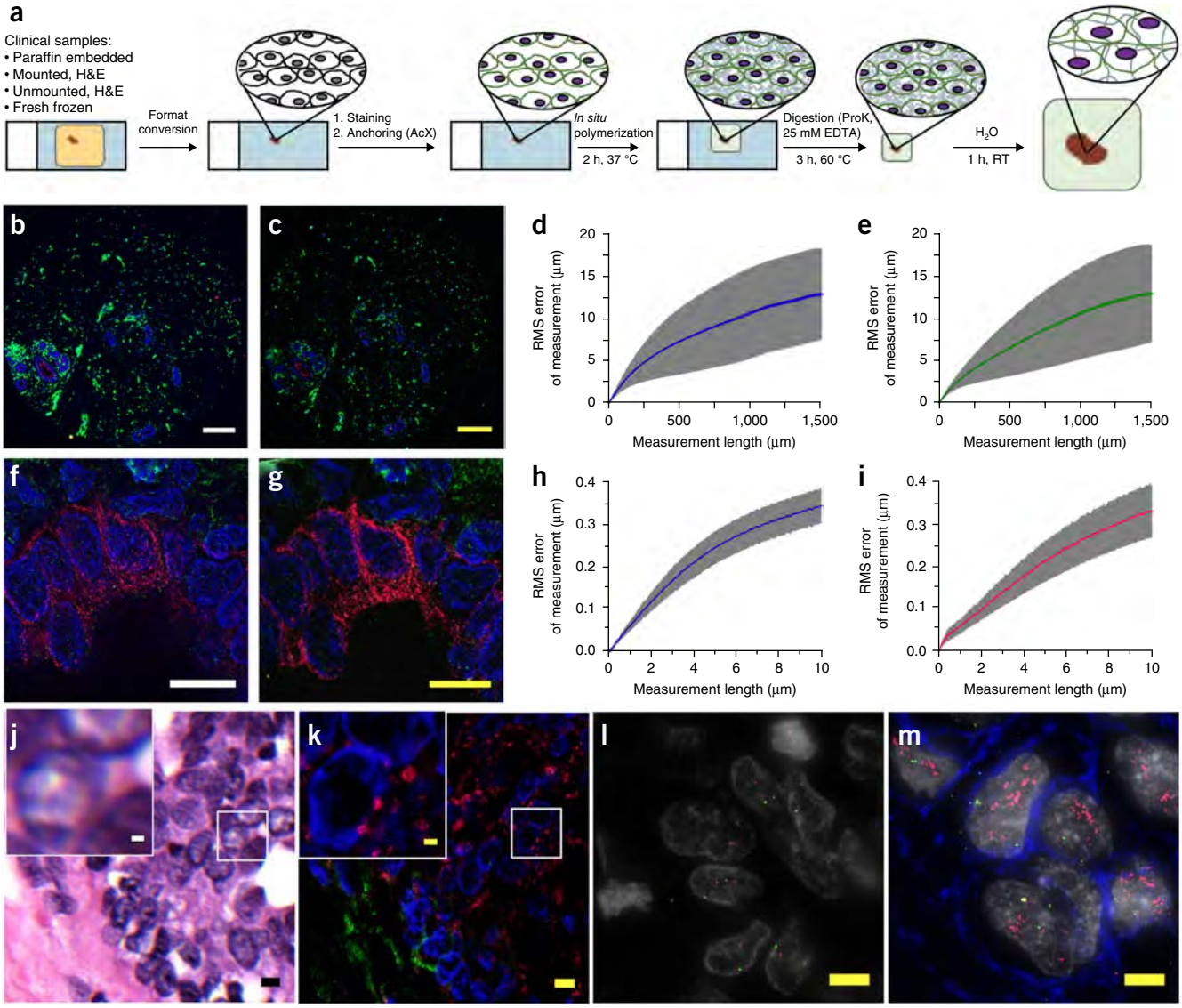

Figure 1 Design and validation of expansion pathology (ExPath) chemical processing. (**a**) Schematic of ExPath workflow (details in **Supplementary Fig. 1**). (**b**) Pre-expansion image of a 1.5-mm core of normal human breast tissue acquired with a wide-field epifluorescent microscope. Blue, DAPI; green, vimentin; magenta, voltage-dependent anion channel (VDAC). (**c**) Postexpansion (i.e., ExPath) wide-field fluorescence image of the sample of **b**. (**d**,**e**) Root mean square (RMS) length measurement error as a function of measurement length for pre-expansion versus postexpansion images (blue solid line, mean of DAPI channel; green solid line, mean of vimentin channel; shaded area, standard error of mean; $n = 3$ samples from different patients; average expansion factor, 4.3 (s.d. 0.3)). (**f**) Super-resolution structured illumination microscopy (SR-SIM) image of normal human breast tissue. Blue, DAPI; green, vimentin; magenta, keratin-19 (KRT19). (**g**) ExPath image of the sample in **f** acquired with a spinning disk confocal microscope. (**h**,**i**) RMS length measurement error as a function of measurement length for ExPath versus SIM images of human breast tissue (blue solid line, mean of DAPI channel; magenta solid line, mean of KRT19 channel; shaded area, standard error of mean; $n = 5$ fields of view from samples from four different patients; average expansion factor, 4.0 (s.d. 0.2)). (**j**) Hematoxylin and eosin (H&E)-stained human breast sample with atypical ductal hyperplasia (ADH). Inset (upper left) is a magnified view of the area framed by the small square at right. (**k**) ExPath wide-field fluorescence image of the sample in **j** stained with antibodies against Hsp60 (magenta) and vimentin (green) and with DAPI (blue). (**l**) ExPath wide-field fluorescence image of a human breast cancer sample without *HER2* amplification. Blue, anti-HER2 (not visible); gray, DAPI; green, DNA FISH against chromosome 17 centrosome; magenta, DNA FISH against HER2. (**m**) ExPath wide-field fluorescence image of a human breast cancer sample with *HER2* amplification, stained as in **l**. Scale bars (yellow scale bars indicate postexpansion images): (**b**) 200 μm; (**c**) 220 μm (physical size postexpansion, 900 μm; expansion factor, 4.1); (**f**) 10 μm; (**g**) 10 μm (physical size postexpansion, 43 μm, expansion factor, 4.3); (**j**) 5 μm, inset 1 μm; (**k**) 5 μm, inset 1 μm (physical size postexpansion, 23 μm; inset, 4.6 μm; expansion factor, 4.6); (**l**) and (**m**), physical size postexpansion 20 μm.

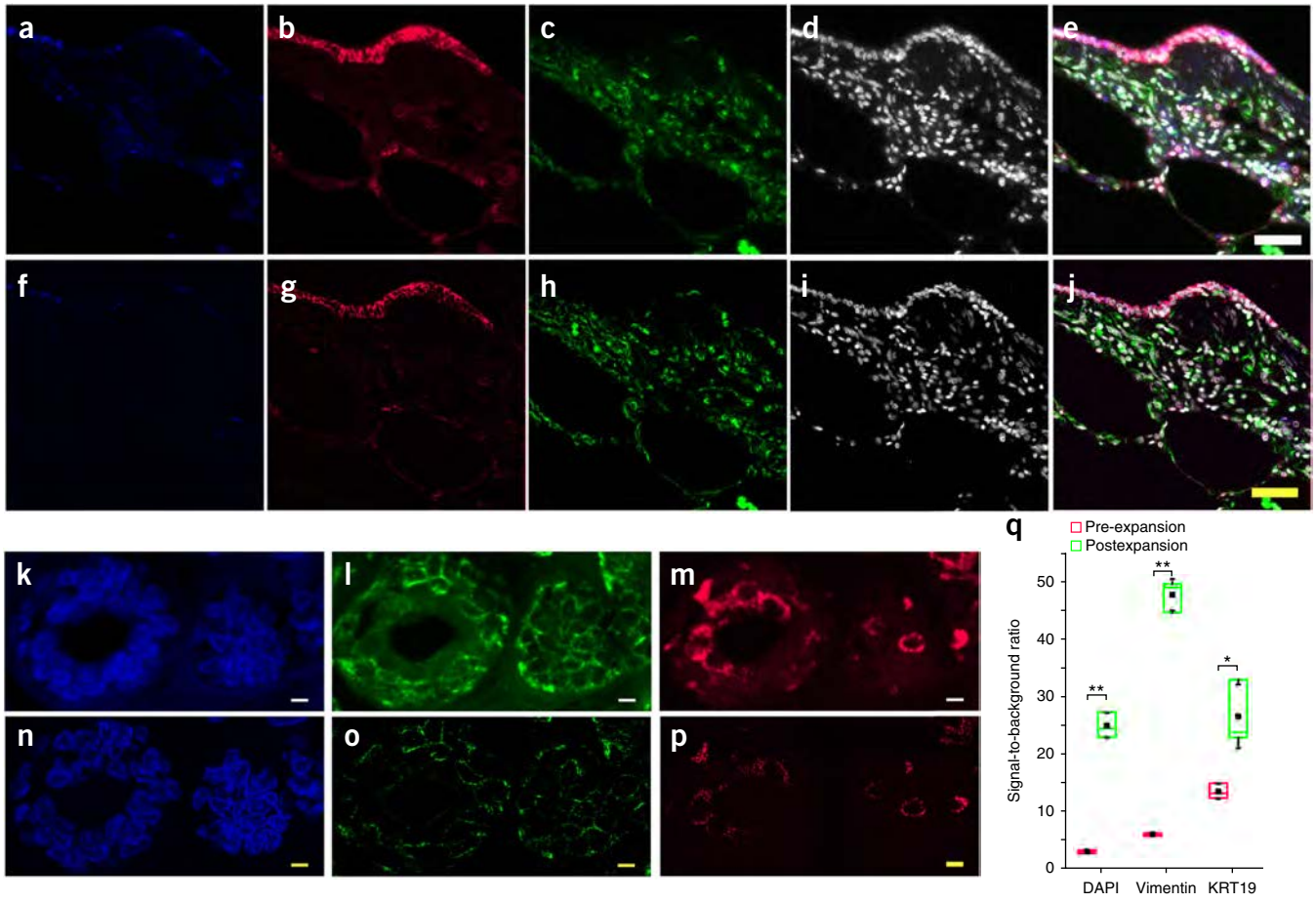

Figure 2 ExPath reduction of tissue autofluorescence. (**a**–**j**) Wide-field images of normal human lung tissue labeled with DAPI (gray) and antibodies against ACTA2 (blue), vimentin (green), and KRT19 (magenta), showing pre-expansion (**a**–**e**) and postexpansion (**f**–**j**) data. (**k**–**p**) Confocal images of normal human breast tissue labeled with DAPI (blue) and antibodies against vimentin (green) and KRT19 (magenta), showing pre-expansion (**k**–**m**) and postexpansion (**n**–**p**) data. (**q**) Signal-to-background ratio for pre-expansion (magenta) as well as postexpansion (green) states of $n = 3$ samples of breast tissue from three patients. Average expansion factor, 4.1 (s.d. 0.1). $^{**}P < 0.01$; $^{*}P < 0.1$, two-tailed paired *t*-test. The ends of whiskers are defined by the s.d.; the upper and lower boundaries of the box are defined by the maximum and minimum, respectively; the segment in the rectangle indicates the median; the square symbol indicates the mean. Scale bars (yellow scale bars indicate postexpansion images): (**e**) 45 µm; (**j**) 45 µm (physical size postexpansion, 208 µm; expansion factor 4.6); (**k**–**m**) 5 µm; (**n**–**p**) 5 µm (physical size postexpansion, 18 µm; expansion factor 4.0).

by rehydration and a fairly standard antigen-retrieval step (placing samples in 20 mM sodium citrate at pH 8 and 100 °C, then immediately transferring the samples into a 60 °C incubator for 30 min; **Supplementary Fig. 1**), could sufficiently prepare FFPE samples for the proExM protocol[9]. In proExM, the succinimidyl ester of 6-((Acryloyl)amino)hexanoic acid (Acryloyl-X, SE; here abbreviated AcX) is used to chemically modify amines on biomolecules with an acrylamide functional group, and this modification enables proteins to be linked to the polymer network; then, polymerization followed by proteinase K digestion (to an extent that spares the proteins of interest, e.g., applied antibodies) and addition of water enables expansion.

We found that heavily formalin-fixed human tissues (e.g., lymph nodes, skin and liver) did not expand evenly under the proExM protocol, even after paraffin removal; but if digestion was performed with 25 mM EDTA versus the 1 mM EDTA used in the original proExM protocol, we obtained excellent isotropic expansion with low autofluorescence (**Supplementary Note; Supplementary Tables 1** and **2**; and **Supplementary Fig. 2a**–**j**). We validated the low distortion obtained by using this protocol on cultured cells using super-resolution structured-illumination (SR-SIM) microscopy pre-expansion and confocal microscopy postexpansion (**Supplementary Fig. 3**). We next validated that this FFPE pipeline, with xylene treatment and increased EDTA, could prepare samples for proExM by assessing the entire pipeline on normal human breast tissues prepared with FFPE preservation. We found that pre-expansion imaging with either a wide-field (**Fig. 1b**) or SR-SIM (**Fig. 1f**) microscope followed by postexpansion imaging on a wide-field (**Fig. 1c**) or confocal (**Fig. 1g**) microscope, respectively, yielded low distortion levels of a few percent over lengthscales of tens to hundreds of microns (**Fig. 1d**,**e**,**h**,**i**), similar to the low distortion levels obtained by earlier ExM protocols[8,9]. Thus, this ExPath protocol expanded paraffin-embedded, highly aldehyde-fixed samples.

We next sought to prepare H&E-stained samples for our enhanced proExM protocol. For mounted samples, we had to remove the coverslip and mounting medium; since we had established that xylene treatment was acceptable as a pretreatment for ExM, we used xylene to remove the coverslip and dissolve the mounting medium (**Supplementary Fig. 1**). H&E-stained tissues exhibited high background fluorescence (**Supplementary Fig. 4**), which suggested that H&E removal would be important for fluorescent antibody staining. We found that both eosin and hematoxylin stains were removed by ExPath processing (**Supplementary Figs. 1** and **4**). We visualized nuclear DNA in postexpansion H&E-stained samples by DAPI

staining (**Fig. 1j**,**k**), and we applied antibody stains against the mitochondrial protein Hsp60 and stromal marker vimentin using an H&E slide of human breast tissue with atypical ductal hyperplasia (ADH). Finally, we evaluated fresh-frozen sections preserved with acetone fixation; we found that lowering the concentration of AcX from 0.1 mg/mL to 0.03 mg/mL enabled more consistent and artifact-free expansion of acetone-fixed samples (**Supplementary Fig. 2k**,**l**), perhaps because of the greater number of free amines in tissues not processed with aldehyde fixatives.

DNA fluorescent *in situ* hybridization (FISH) is commonly used to assess *ERBB2* (*HER2*) gene amplification in breast cancer. We recently developed a method for expanding RNAs away from each other in biological samples and then accurately imaging their identity and location with RNA FISH[12]; here, we examined whether postexpansion DNA FISH was possible. The large size of traditional bacterial artificial chromosome (BAC)-based FISH probes (the length of BAC-based FISH probes targeting *HER2* is approximately 220 kb) precludes efficient delivery to expanded samples, so we used commercially available SureFISH probes, which are libraries of single-stranded oligonucleotides with an average size of ~150 bases[13], targeting *HER2* and (as a control) the centrosome of chromosome 17. We observed that SureFISH probes diffused into breast ExPath samples and hybridized with chromosomal DNA for specimens of breast cancers with no amplification of *HER2* (**Fig. 1l**) and for breast cancers with *HER2* amplification (**Fig. 1m**); more DNA hybridization was apparent in the *HER2*-amplified case. As DNA FISH is performed in the final step of the process, it does not interfere with immunostaining earlier in the protocol. We costained the breast samples with an antibody against HER2 protein, and we confirmed the correlation of HER2 protein expression with *HER2* gene amplification (**Fig. 1l**,**m**).

Because ExPath spaces molecules apart and results in elimination of unanchored or digested molecules (such as nonantibody proteins that are digested by proteinase K treatment), this technique has several advantages over conventional immunostaining. For example, tissue autofluorescence remains challenging for clinical applications of immunofluorescence and FISH in pathology analysis, despite existing autofluorescence reduction methods[14–16]. Specimens processed with ExPath are >99% water and are thus transparent and refractive-index matched to water. We observed substantially reduced autofluorescence from lung (**Fig. 2a–j**, wide-field fluorescence images) and breast (**Fig. 2k–p**, confocal fluorescence images) ExPath-processed specimens when we compared signal-to-background ratios (from regions selected by a pathologist's visual inspection) in spectral channels ranging from UV to red (**Fig. 2q**, $n = 3$ normal breast samples from different patients). Thus, the molecular clearing of ExPath, which eliminates unanchored biomolecules (potentially including both proteins and small molecules) that contribute to autofluorescence, can reduce autofluorescence by an order of magnitude in some spectral channels.

We applied ExPath to tissue microarrays containing specimens from various organs, including normal and cancer-containing tissues from breast, prostate, lung, colon, pancreas, kidney, liver and ovary (**Fig. 3**); in all cases we obtained expansions of ~4–5×, with an average expansion factor of 4.7 (s.d. 0.2; **Supplementary Table 3**). The expansion variation for the specimens noted above was smaller than 10%, which indicates consistent expansion performance across different types of human tissue. ExPath revealed sub-diffraction-limit-sized features of the intermediate filaments keratin and vimentin, which are critical in the epithelial–mesenchymal transition[17], cancer progression and initiation of metastasis[18] (**Fig. 3**). An interesting future direction for ExPath will be the examination of the nanoscale architecture of these and other proteins in the cellular and tissue context of cancer. We anticipate that ExPath will provide a simple and convenient way to observe nanoscale morphology of both nucleic

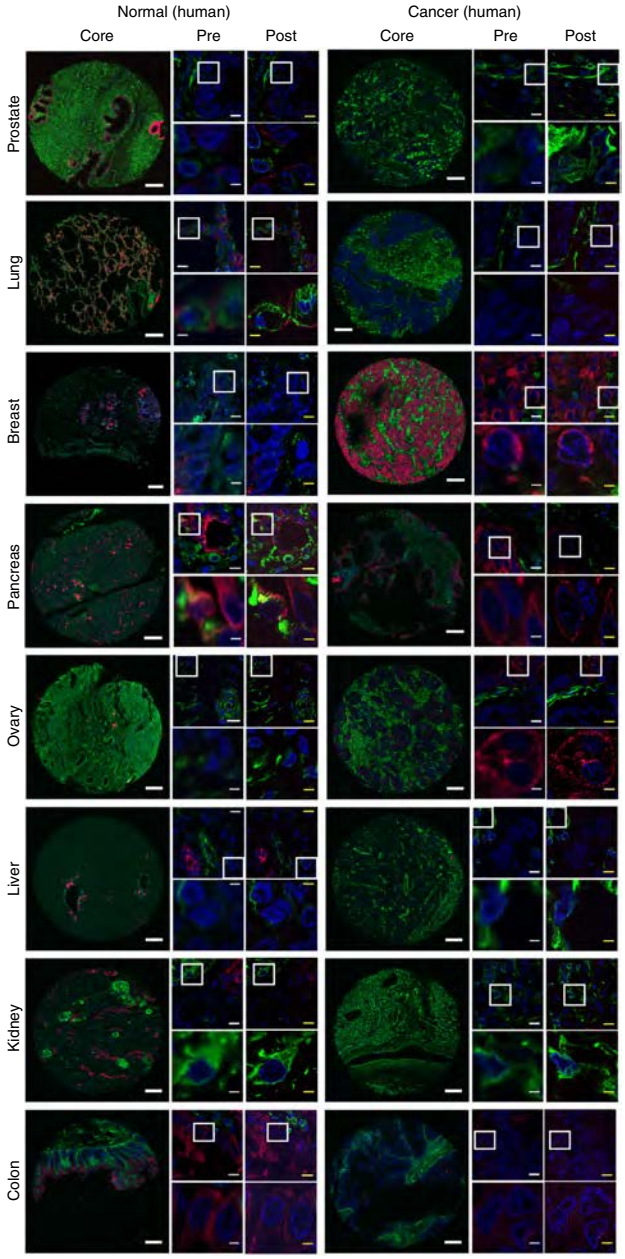

Figure 3 ExPath imaging of a wide range of human tissue types. Images of various tissue types for both normal (left images) and cancerous (right images) tissues from human patients. From top to bottom, different rows show different tissue types as labeled (e.g., prostate, lung, breast, etc.). Within each block of images for a given tissue *x* disease type, there are five images shown. The left-most of the five images shows a core from a tissue microarray (scale bar, 200 μm). The middle column within the five images shows two images, the top of which is a small field of view (scale bar, 10 μm), and the bottom of which zooms into the area outlined in the top image by a white box (scale bar, 2.5 μm). The right column within the five images shows the same fields of view as are shown in the middle column, but postexpansion (yellow scale bars: top images, 10–12.5 μm; bottom images, 2.5–3.1 μm. Physical size postexpansion: top images, 50 μm; bottom images, 12.5 μm; expansion factors 4.0–5.0×; see **Supplementary Table 3** for raw data). Blue, DAPI; green, vimentin; magenta, KRT19.

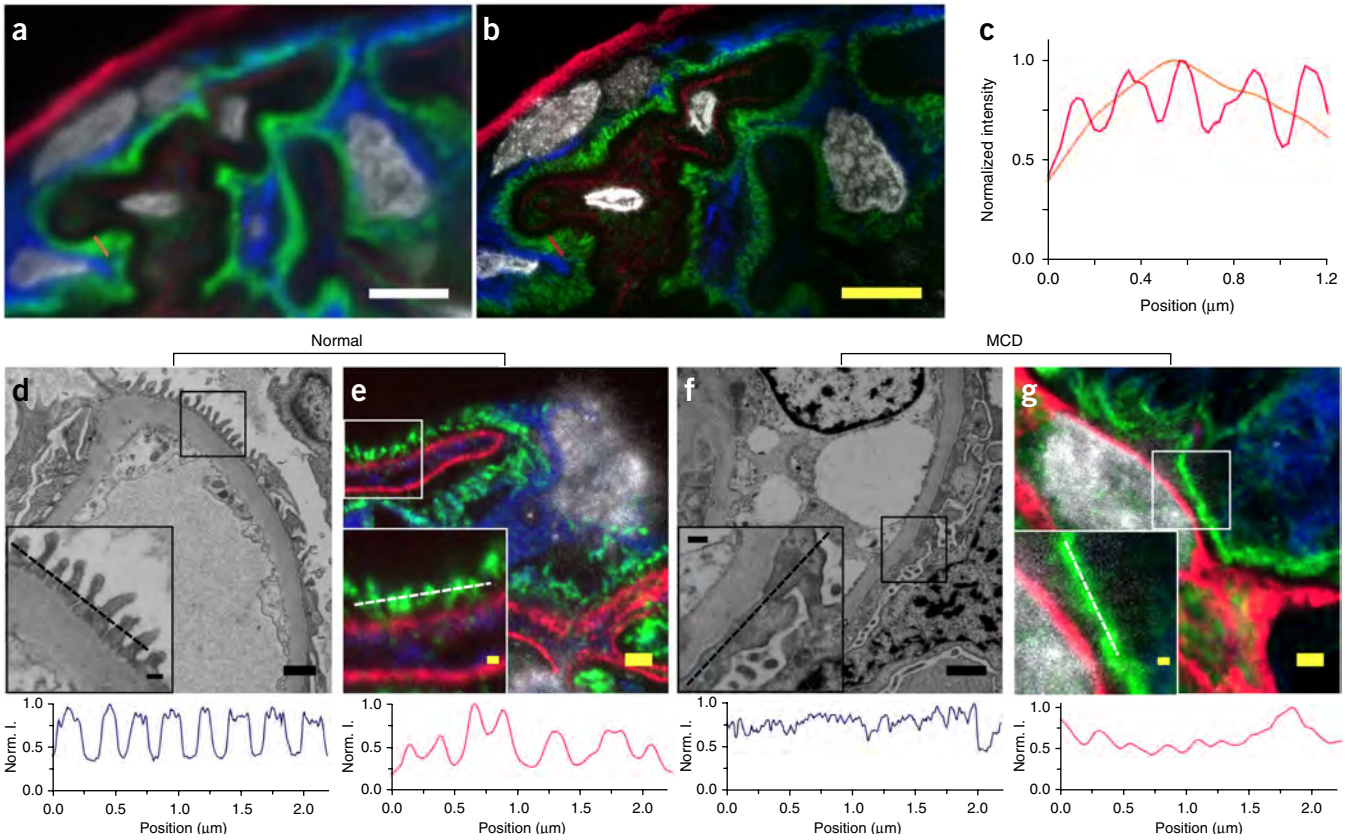

Figure 4 ExPath analysis of kidney podocyte foot process effacement. (**a**) Pre-expansion confocal image of a normal human kidney sample showing part of a glomerulus acquired with a spinning disk confocal microscope. Blue, vimentin; green, actinin-4; magenta, collagen IV; gray, DAPI. Orange line indicates the line cut analyzed in **c**. (**b**) ExPath image of the sample in **a** using the same microscope. Red line indicates the line cut analyzed in **c**. (**c**) Profiles of actinin-4 intensity along the orange and Red dotted lines of **a** and **b**. (**d**) Electron micrograph of a clinical biopsy sample from a normal human kidney. Inset, zoom into the region outlined by the black box; dotted line within the inset indicates the line cut analyzed in the graph below the image. Below, electron micrograph feature intensity along the line cut of the inset, normalized to maximum intensity (Norm. I.). (**e**) ExPath image of a clinical kidney biopsy sample from the same patient analyzed in **d**, stained as in **a**. Inset, zoom into the region outlined by the white box; dotted line within the inset indicates the line cut analyzed below. Below, actinin-4 intensity along the line cut of the inset, normalized as in **d**. (**f**) As in **d**, but for a patient with minimal change disease (MCD). (**g**) As in **e**, but for the same patient as in **f**. Scale bars (yellow indicates a postexpansion image): (**a**) 5 μm; (**b**) 5 μm (physical size postexpansion, 23.5 μm; expansion factor, 4.7); (**d**) 1 μm; inset, 200 nm; (**e**) 1 μm (physical size postexpansion, 4.3 μm; expansion factor, 4.3); inset, 200 nm; (**f**) 1 μm, inset, 200 nm; (**g**) 1 μm (physical size postexpansion, 4.2 μm; expansion factor, 4.2); inset, 200 nm.

acids and protein biomarkers in clinical biopsy samples from a wide range of human organs.

Expansion pathology enables visualization of human podocyte tertiary foot processes

Many potential uses of ExPath will likely be discovered by future exploration of normal versus abnormal samples followed by traditional or automated inspection of key features for both pinpointing novel pathological mechanisms and for disease classification and refined diagnosis. However, there are some scenarios where nanoscopic resolution is already necessary. For example, nephrotic kidney diseases such as MCD and focal segmental glomerulosclerosis (FSGS) are typically diagnosed or confirmed via EM[19,20]. In MCD, kidney tertiary podocyte foot processes, which normally cover the surface of glomerular capillary loops like interdigitating fingers, lose their characteristic morphology and appear continuous under EM—a phenomenon called foot process effacement[10]. The width of individual foot processes is around 200 nm, which is beyond the resolution of conventional optical microscopy[21].

Here, we explored whether ExPath could enable imaging of podocyte foot processes (**Fig. 4**). We identified both an anti-actinin-4 (ref. 22) and an anti-synaptopodin[23] antibody, each of which could specifically label tertiary podocyte foot processes in acetone-fixed frozen kidney samples that were heat treated before immunostaining (**Supplementary Figs. 5** and **6**). Compared with the immunostaining quality of acetone-fixed frozen kidney samples, that of FFPE-preserved samples decreased slightly for anti-actinin-4 staining (**Supplementary Fig. 7**)—a difference that was presumably a result of degraded actinin-4 antigenicity caused by formalin. We stained human kidney samples with anti-actinin-4, antibodies against vimentin (a glomerular marker) and collagen IV (a capillary basement membrane marker); and we successfully observed the microanatomy of glomeruli in normal human kidney samples (**Fig. 4a**,**b**) postexpansion, revealing ultrafine structures of tertiary podocyte foot processes (**Fig. 4b**,**c**) not visible in confocal imaging (**Fig. 4a**). We acquired ExPath images of fresh-frozen kidney sections from individuals with normal kidneys as well as from patients with MCD and FSGS. We observed the ultrafine structure of tertiary foot processes in kidneys from normal cases (**Fig. 4e**) and foot process effacement in MCD cases (**Fig. 4g**), consistent with the morphologies seen in EM images from the same samples (**Fig. 4d**,**f**). Thus, with ExPath, nanoscale

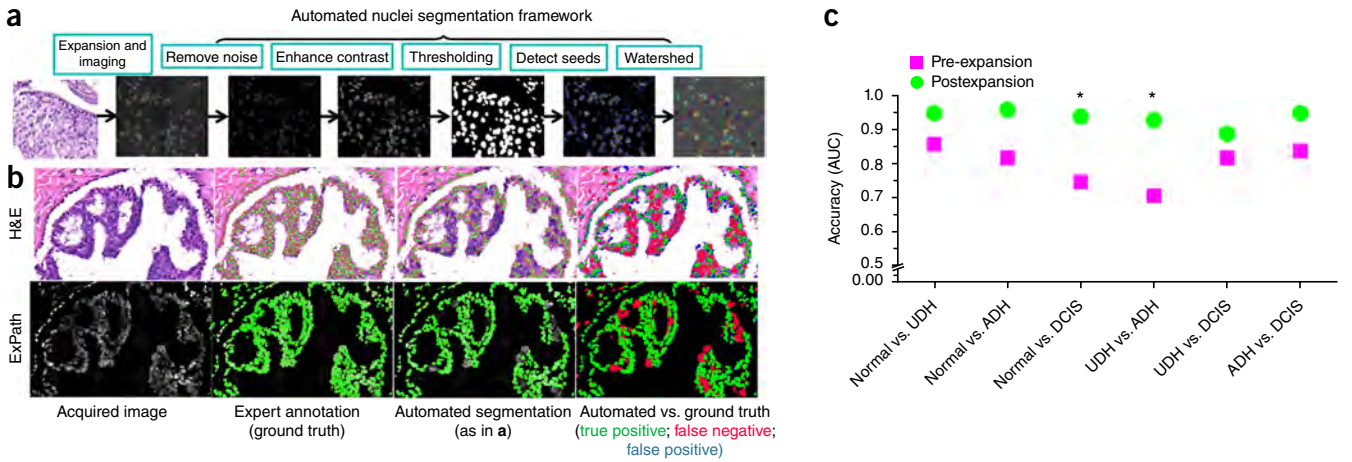

Figure 5 ExPath improvement of computational diagnosis of early breast lesions. (**a**) Automated nucleus segmentation framework, showing steps of the image preprocessing and nuclei segmentation pipeline. From left to right, noise removal using rolling-ball correction, enhancing contrast by histogram equalization, nucleus segmentation by minimum error thresholding, seed detection by multiscale Laplacian of Gaussian (LoG) filter, nuclei splitting by marker-controlled watershed. (**b**) Computational detection and segmentation of nuclei is significantly more accurate in expanded versus pre-expanded samples; example of atypical ductal hyperplasia (ADH). For the "Expert annotation" and "Automated segmentation" columns, green-filled nuclei are nuclei segmented by the expert or the automated segmentation algorithm, respectively (red circles indicate nucleus outlines, which are not visible in the ExPath row because the resolution is too high, and thus the outline is barely visible). In the "automated vs. ground truth" column, green-filled nuclei, true positives; red-filled nuclei, false negatives; blue-filled nuclei, false positives (note that when the automated segmentation yielded larger outlines than the expert, this was expressed as a blue 'halo' around the green). (**c**) Classification models were built using L1-regularized logistic regression (the GLMNET classifier). Classification accuracy was measured as the area under the receiver operator curve (AUC) achieved by the classification model in cross-validation. We applied this image classification framework on both pre-expanded H&E and postexpanded DAPI images for computational differentiation of normal, benign and preinvasive malignant breast diseases. Both data sets consisted of 105 images that contained 36 normal breast tissue images, 31 benign breast tissue images (15 UDH and 16 ADH) and 38 noninvasive breast cancer tissue images (DCIS). Average expansion factor, 4.8 (s.d. 0.3). $^*P < 0.05$; bootstrapped paired *t*-test. *P* value for each binary comparison: normal versus UDH, 0.17; normal versus ADH, 0.34; normal versus DCIS, 0.24; UDH versus ADH, 0.02; UDH versus DCIS, 0.01; ADH versus DCIS, 0.24.

differences between clinical samples of nephrotic diseases can be visualized with diffraction-limited optical microscopes.

To examine in a blinded study whether ExPath could enable accurate identification of foot process effacement in MCD and FSGS cases, seven observers—four pathologists and three nonpathologists—first studied a training set of immunofluorescence images of kidney glomeruli in both pre-expansion and postexpansion states (see full image set in **Supplementary Fig. 8**); then they examined ten pre-expansion and ten postexpansion immunofluorescence images of kidney glomeruli from three specimens from normal subjects, two specimens from MCD patients and one specimen from an FSGS patient (**Supplementary Fig. 8** and **Supplementary Table 4**). For unexpanded samples, classification accuracy was only 65.7% (s.d. 17%), but accuracy increased significantly to 90% (s.d. 8%) when ExPath samples were used ($P = 0.0088$, $n = 7$ individuals, two-tailed *t*-test; raw data in **Supplementary Table 5**). To assess interobserver agreement, we calculated Fleiss's kappa values for observers' categorical ratings on pre-expansion versus postexpansion images. Observers' ratings of postexpansion data were in substantial agreement, with kappa value 0.68 ± 0.14 at the 95% confidence level; whereas interobserver agreement was poor on pre-expansion data (0.35 ± 0.13, 95% confidence level; this value was borderline, given the clinically acceptable threshold of 0.40)[24]. ExPath enabled accurate and consistent evaluation between observers on whether the image was from a sample in a normal or abnormal state from a single postexpansion image (in clinical practice, kidney pathologists normally examine multiple EM images for diagnosis). Large-scale blinded studies using ExPath—although these are beyond the scope of the current technology-oriented paper—will be required to determine whether ExPath can streamline the diagnosis or confirmation of nephrotic kidney disease and other diseases that involve known nanoscale pathology.

Expansion pathology improves computational diagnosis in early breast lesions

To further explore the utility of ExPath, we examined the pathological classification of early breast lesions, which represents one of the most challenging problem areas in breast pathology[11]. For example, one study has shown that there is only ~50% agreement between pathologists for nuclear atypia diagnosis in early breast lesions[11]. The classification of these lesions provides diagnostic information that is critical for preventing overtreatment and undertreatment and for guiding clinical management[25,26].

We hypothesized that the problems with the current classification schemes are due to two issues—first, the diagnostic criteria are largely qualitative and subjective; second, the information contained in the images is limited by the optical diffraction limit of conventional optical microscopes. To start addressing the first issue, we previously developed computational pathology models that can discriminate benign from malignant intraductal proliferative breast lesions[27]. However, the efficacy of these models is limited by the information extractable from diffraction-limited images. Because ExPath substantially increases image resolution, we anticipated that the extra information made accessible by ExPath could lead to a higher quality of extracted features and thus improve the classification of preinvasive breast lesions.

We applied our previously developed image classification framework[27] to ordinary H&E-stained samples, and we applied an image classification framework updated with nucleus detection and segmentation algorithms optimized for postexpansion DAPI-stained images (**Fig. 5a**) to expanded samples. Our image classification framework

for postexpansion DAPI-stained images included foreground detection, nucleus seed detection and nuclear segmentation (**Fig. 5a**). Following application of this framework, we extracted three kinds of features from each segmented nucleus from both the pre-expanded and postexpanded images—nuclear morphology features, nuclear intensity features and nuclear texture features.

Each of the two data sets (pre-expansion and postexpansion) consisted of 105 images—36 normal breast tissue images, 31 proliferative lesion (benign) images (15 usual ductal hyperplasia, (UDH) and 16 atypical ductal hyperplasia (ADH)) and 38 ductal carcinoma *in situ* (DCIS). The average expansion factor was 4.8 (s.d. 0.3). We first assessed the impact of ExPath on nuclear detection and segmentation for a subset of 31 images (6 normal, 9 UDH, 9 ADH and 7 DCIS; **Fig. 5b**). Computational detection of nuclei was significantly more accurate in expanded samples (**Fig. 5b**), with an 11% increase in true-positive rate, a 22% increase in positive predictive value, and a 16% increase in F-score over nonexpanded samples (**Supplementary Tables 6** and **7**; **Supplementary Fig. 9**); and segmentation was significantly improved as well, with a 14% increase in F-score, a 77% increase in Cohen's kappa and a 66% decrease in global consistency error (GCE) (**Supplementary Table 8**). This improved accuracy of nuclear detection and segmentation could in principle support improved computational pathology analyses. To this end, we found that expansion substantially improved the performance of diagnosis classification models over pre-expansion data (**Fig. 5c** and **Supplementary Table 9**). When we examined the area under the receiver operator curve (AUC) of true positives versus false positives (a perfect classifier would achieve an AUC of 1, and a random classifier would achieve an AUC of 0.5), our pipeline could discriminate lesions such as UDH from atypical lesions such as ADH with an AUC of 0.93 on expanded samples compared with only 0.71 on pre-expanded samples. The most significant features selected by these classification models are shown in **Supplementary Tables 10** and **11**. Features extracted from individual postexpansion images were normalized by their expansion factors before running our digital pathology pipeline; however, such normalization did not greatly affect the results (**Supplementary Table 12**). These findings suggest that the improved nuclear segmentation achieved on postexpansion images results in more informative features and, in turn, more accurate classification models.

DISCUSSION

We herein describe ExPath, a simple and versatile method for optical interrogation of clinical biopsy samples with nanoscale precision and molecular information. ExPath is an extension of our proExM protocol[9] optimized for clinical samples—FFPE, H&E-stained and fresh-frozen tissues. ExPath thus enables nanoscale imaging of clinical samples on common imaging hardware. We found that ExPath functions well on a wide diversity of tissue types, and that it has immediate clinical application in the diagnosis of diseases known to exhibit nanoscale pathology (e.g., kidney MCD). Although EM has far superior resolution to that of ExPath, the processing time for ExPath is significantly shorter than that for EM, and the skills and equipment required to perform ExPath are less demanding than those required for EM (**Supplementary Table 13**). Moreover, ExPath enables multiplexed localization and identification of biomolecules *in situ*, both of which are challenging with EM. Of course, without larger scale studies it is unclear whether ExM would eliminate the need for EM in diagnostic renal pathology of podocytopathies. We highlight the potential of ExPath to improve diagnostics by providing greater information content to inform sample classification. We found that ExPath enhances researchers' ability to detect and segment nuclei, and that the increased information content of expanded breast tissue samples improves the performance of computational pathology classifiers for the analysis of proliferative breast lesions.

ExM protocols are robust; in parallel to our development of proExM, two other groups developed related protocols[28,29]; this highlights the ability of multiple groups to implement such technologies. Another key advantage of ExPath is its versatility; we demonstrate here that not only can ExPath address a wide variety of samples, but also it can be used for multimodal investigation of clinical samples (e.g., incorporating DNA FISH into the pipeline, using only commercially available probes). In the future, it will be of interest to researchers and clinicians to combine ExPath with ongoing developments in multiplexed imaging of RNA[30–32] and protein[33]. Although embedding biological specimens in hydrogels such as polyacrylamide to support imaging goes back decades[34], the use of polyelectrolyte hydrogels to move biomolecules and labels apart evenly not only helps improve the resolution of existing microscopes, but also may help support chemical analysis of biomolecules *in situ*, since ExM separates biomolecules and surrounds them with pure environments of our choosing.

In the current iteration, ExPath enables ~4.5× physical magnification in each dimension. Although it expands the volume to be imaged, and thus requires more voxels to be imaged, the ability to use fast diffraction-limited optics enables the voxel sizes of a super-resolution imaging modality to be acquired at the voxel acquisition rates of fast diffraction-limited optics. ExPath is compatible with a wide variety of stains and antibodies used throughout biology and pathology. Similar to those of ExM and proExM, ExPath samples are transparent with a refractive index matched to that of water, and they can thus support fast volumetric imaging on light-sheet microscopes (as has been previously shown for expanded samples[12]). In the current implementation of ExPath, most proteins are digested away to enable even expansion, and this prevents postexpansion interrogation. In the future, protein-retention forms of ExM that enable most proteins to be retained[9,29] may support more information-preserving forms of ExPath. To date, these 'full protein retention' forms of ExM have not been fully validated by direct comparison to a classical super-resolution modality. Another property of ExPath is that the expansion process dilutes the concentration of fluorophores. For low-abundance targets, it may be desirable to implement signal amplification before imaging. Since proteins are lost after proteinase K treatment, non-protein-reliant amplification methods such as hybridization chain reaction amplification of gel-anchored labels may be helpful, as has been demonstrated for single-molecule RNA imaging in expanded specimens[12].

Standardization and automation of ExPath are important future steps toward clinical adoption. Comparing pre-expansion and postexpansion images taken at low magnifications enables simple calculation of the expansion factor, so that the physical size of the postexpansion image can be mapped onto biologically relevant units, and nulling out the small (<10%) sample-to-sample expansion factor variation.

ExPath may broadly enhance the computational analysis of pathological specimens. Here, we analyzed nuclear morphology and explored the classification of early breast lesions. We found that nuclear segmentation algorithms, which historically have shown only moderate performance on standard histopathological images[35], show excellent performance on ExPath images. We also found that diagnosis classification models that focus on nuclear morphologic phenotypes perform better on ExPath images than on pre-expansion images. The accurate classification of preinvasive breast diseases represents a difficult area in diagnostic pathology with significant discordance observed between individual pathologists[11]. Accurate classification is

important because it determines clinical treatment which can range from observation (for a benign, nonatypical lesion) to surgery (for a diagnosis of atypia or malignancy). Further validation of our findings on larger sample sets will be critical for understanding the potential of this technology in the clinic. In general, as cancer screening procedures for common malignancies (e.g., malignancies in skin, lung, prostate, esophagus and colon) continue to improve, a larger proportion of pathology specimens will contain small, noninvasive lesions, and accurate pathological classification of these specimens will play an important role in clinical management.

METHODS

Methods, including statements of data availability and any associated accession codes and references, are available in the online version of the paper.

Note: Any Supplementary Information and Source Data files are available in the online version of the paper.

ACKNOWLEDGMENTS

For funding, E.S.B. acknowledges the MIT Media Lab; the Open Philanthropy project; the HHMI-Simons Faculty Scholars Program; the US Army Research Laboratory and the US Army Research Office under contract/grant number W911NF1510548; the MIT Brain and Cognitive Sciences Department; the New York Stem Cell Foundation-Robertson Investigator Award; NIH Transformative Award 1R01GM104948; NIH Director's Pioneer Award 1DP1NS087724; NIH 1R01EY023173; NIH 1U01MH106011; NIH 1R01MH110932; and the MIT McGovern Institute MINT program. A.H.B. acknowledges support from Harvard Catalyst, the Harvard Clinical and Translational Science Center (National Center for Research Resources and the National Center for Advancing Translational Sciences, National Institutes of Health Award UL1 TR001102), and financial contributions from Harvard University and its affiliated academic healthcare centers. A.H.B. and O.B. also acknowledge support from the Ludwig Center at Harvard and the Ludwig's members J. Brugge and J. Staunton. O.B. acknowledges the Lady Tata Memorial Trust, London. F.C. acknowledges the NSF Fellowship and Poitras Fellowship.

AUTHOR CONTRIBUTIONS

Y.Z., O.B., A.H.B. and E.S.B. all contributed key ideas, designed experiments and analyzed data. F.C. and Y.Z. performed SR-SIM experiments on tissues. Y.Z. and O.B. designed and acquired ExPath data for all tissues. H.I., O.B. and Y.Z. analyzed ExPath data for breast benign neoplasia experiments. H.I. developed the computational image analysis framework for the breast benign neoplasia analysis. A.L.S. performed the expert annotation (ground truth) for the image analysis framework. E.-Y.O., S.J.S. and B.G. performed the selection and annotation of the breast lesions. A.W., M.D., V.T. and I.E.S. participated in the single blinded test for the ExPath kidney experiment. All authors contributed to the writing of the manuscript. A.H.B. and E.S.B. supervised the project.

COMPETING FINANCIAL INTERESTS

The authors declare competing financial interests: details are available in the online version of the paper.

1. Huang, B., Bates, M. & Zhuang, X. Super-resolution fluorescence microscopy. *Annu. Rev. Biochem.* **78**, 993–1016 (2009).
2. Huang, B., Babcock, H. & Zhuang, X. Breaking the diffraction barrier: super-resolution imaging of cells. *Cell* **143**, 1047–1058 (2010).
3. Hell, S.W. Far-field optical nanoscopy. In *2010 23rd Annual Meeting of the IEEE Photonics Society* (ed. Novak, D.) 3–4 (IEEE, 2010).
4. Hell, S.W. Toward fluorescence nanoscopy. *Nat. Biotechnol.* **21**, 1347–1355 (2003).
5. Phelps, P.E., Houser, C.R. & Vaughn, J.E. Immunocytochemical localization of choline acetyltransferase within the rat neostriatum: a correlated light and electron microscopic study of cholinergic neurons and synapses. *J. Comp. Neurol.* **238**, 286–307 (1985).
6. Nixon, R.A. *et al.* Extensive involvement of autophagy in Alzheimer disease: an immuno-electron microscopy study. *J. Neuropathol. Exp. Neurol.* **64**, 113–122 (2005).
7. Gaietta, G. *et al.* Multicolor and electron microscopic imaging of connexin trafficking. *Science* **296**, 503–507 (2002).
8. Chen, F., Tillberg, P.W. & Boyden, E.S. Expansion microscopy. *Science* **347**, 543–548 (2015).
9. Tillberg, P.W. *et al.* Protein-retention expansion microscopy of cells and tissues labeled using standard fluorescent proteins and antibodies. *Nat. Biotechnol.* **34**, 987–992 (2016).
10. Waldman, M. *et al.* Adult minimal-change disease: clinical characteristics, treatment, and outcomes. *Clin. J. Am. Soc. Nephrol.* **2**, 445–453 (2007).
11. Elmore, J.G. *et al.* Diagnostic concordance among pathologists interpreting breast biopsy specimens. *J. Am. Med. Assoc.* **313**, 1122–1132 (2015).
12. Chen, F. *et al.* Nanoscale imaging of RNA with expansion microscopy. *Nat. Methods* **13**, 679–684 (2016).
13. Leproust, E.M., Chen, S. & Ruvolo, M. Synthesis of long fish probes. US patent 20140256575 A1 (2014).
14. Schnell, S.A., Staines, W.A. & Wessendorf, M.W. Reduction of lipofuscin-like autofluorescence in fluorescently labeled tissue. *J. Histochem. Cytochem.* **47**, 719–730 (1999).
15. Viegas, M.S., Martins, T.C., Seco, F. & do Carmo, A. An improved and cost-effective methodology for the reduction of autofluorescence in direct immunofluorescence studies on formalin-fixed paraffin-embedded tissues. *Eur. J. Histochem.* **51**, 59–66 (2007).
16. Neumann, M. & Gabel, D. Simple method for reduction of autofluorescence in fluorescence microscopy. *J. Histochem. Cytochem.* **50**, 437–439 (2002).
17. Mendez, M.G., Kojima, S. & Goldman, R.D. Vimentin induces changes in cell shape, motility, and adhesion during the epithelial to mesenchymal transition. *FASEB J.* **24**, 1838–1851 (2010).
18. Maier, J., Traenkle, B. & Rothbauer, U. Real-time analysis of epithelial–mesenchymal transition using fluorescent single-domain antibodies. *Sci. Rep.* **5**, 13402 (2015).
19. Pease, D.C. Fine structures of the kidney seen by electron microscopy. *J. Histochem. Cytochem.* **3**, 295–308 (1955).
20. Ranganathan, S. Pathology of podocytopathies causing nephrotic syndrome in children. *Front Pediatr.* **4**, 32 (2016).
21. Hirose, T. *et al.* An essential role of the universal polarity protein, aPKClambda, on the maintenance of podocyte slit diaphragms. *PLoS One* **4**, e4194 (2009).
22. Dandapani, S.V. *et al.* Alpha-actinin-4 is required for normal podocyte adhesion. *J. Biol. Chem.* **282**, 467–477 (2007).
23. Mundel, P. *et al.* Synaptopodin: an actin-associated protein in telencephalic dendrites and renal podocytes. *J. Cell Biol.* **139**, 193–204 (1997).
24. Sim, J. & Wright, C.C. The kappa statistic in reliability studies: use, interpretation, and sample size requirements. *Phys. Ther.* **85**, 257–268 (2005).
25. Degnim, A.C. *et al.* Gene signature model for breast cancer risk prediction for women with sclerosing adenosis. *Breast Cancer Res. Treat.* **152**, 687–694 (2015).
26. Allison, K.H. *et al.* Understanding diagnostic variability in breast pathology: lessons learned from an expert consensus review panel. *Histopathology* **65**, 240–251 (2014).
27. Dong, F. *et al.* Computational pathology to discriminate benign from malignant intraductal proliferations of the breast. *PLoS One* **9**, e114885 (2014).
28. Chozinski, T.J. *et al.* Expansion microscopy with conventional antibodies and fluorescent proteins. *Nat. Methods* **13**, 485–488 (2016).
29. Ku, T. *et al.* Multiplexed and scalable super-resolution imaging of three-dimensional protein localization in size-adjustable tissues. *Nat. Biotechnol.* **34**, 973–981 (2016).
30. Lubeck, E. & Cai, L. Single-cell systems biology by super-resolution imaging and combinatorial labeling. *Nat. Methods* **9**, 743–748 (2012).
31. Lubeck, E., Coskun, A.F., Zhiyentayev, T., Ahmad, M. & Cai, L. Single-cell *in situ* RNA profiling by sequential hybridization. *Nat. Methods* **11**, 360–361 (2014).
32. Chen, K.H., Boettiger, A.N., Moffitt, J.R., Wang, S. & Zhuang, X. RNA imaging. Spatially resolved, highly multiplexed RNA profiling in single cells. *Science* **348**, aaa6090 (2015).
33. Jungmann, R. *et al.* Multiplexed 3D cellular super-resolution imaging with DNA-PAINT and Exchange-PAINT. *Nat. Methods* **11**, 313–318 (2014).
34. Germroth, P.G., Gourdie, R.G. & Thompson, R.P. Confocal microscopy of thick sections from acrylamide gel embedded embryos. *Microsc. Res. Tech.* **30**, 513–520 (1995).
35. Irshad, H., Veillard, A., Roux, L. & Racoceanu, D. Methods for nuclei detection, segmentation, and classification in digital histopathology: a review-current status and future potential. *IEEE Rev. Biomed. Eng.* **7**, 97–114 (2014).

ONLINE METHODS

Human samples. The breast pathological specimens used in **Figure 1j**,**k** and nine cases from the study on ExPath-based analysis of early breast lesions (**Fig. 5**) were from the pathology archives of the Beth Israel Deaconess Medical Center, obtained under BIDMC IRB protocol #2013p000410 to A.H.B. (in addition, we used 11 cases from US Biomax and 21 cases from Abcam). The frozen kidney pathological samples used in **Figure 4d–g** and **Supplementary Figure 8** were provided by the Brigham and Women's Hospital archives under the BWH IRB protocol #2011P002692 to A.W. The rest of the breast and kidney samples used in this study were bought from either US Biomax or Abcam (**Supplementary Table 14**). Other human tissue samples and tissue microarrays were purchased from commercial sources (see **Supplementary Table 14**). The use of unused, unidentified archival specimens does not require informed consent from the subjects.

Tissue section recovery. For formalin-fixed paraffin-embedded (FFPE) clinical samples, samples were sequentially placed in a series of solutions: 2× xylene, 2× 100% ethanol, 95% ethanol, 70% ethanol, 50% ethanol and (finally) doubly deionized water. All of these steps were performed at room temperature (RT), 3 min each.

For stained and mounted permanent slides, samples were briefly placed in xylene at RT. Then coverslips were carefully removed with appropriate tools, such as a razor blade. If the coverslip was difficult to remove, the slides were further incubated in xylene at RT until the coverslip was loosened. Slides were then treated as FFPE samples.

Unfixed frozen tissue slides in optimum cutting temperature (OCT) solution (Tissue-Tek) were initially fixed for 10 min in acetone at −20 °C before three PBS washes for 10 min each at RT. For already fixed frozen clinical tissue sections, the slides were left at RT for 2 min to let the OCT melt and washed 3× with PBS solution at RT for 5 min each.

Sample heat treatment. All human tissue samples used in this study were heat treated before immunostaining. Briefly, tissue slides were placed in 20 mM sodium citrate solution (pH 8, when measured at RT) at ~100 °C in a heat-resistant container, and then the container was immediately transferred to a 60 °C incubator for 30 min.

Immunostaining. Samples were first blocked with MAXblock Blocking Medium (Active Motif) for 1 h at 37 °C, followed by incubation with primary antibodies in MAXbind Staining Medium (Active Motif) at a concentration of 10 μg/mL for at least 3 h at RT or 37 °C (in our hands, it did not matter which), and then washed three times with MAXwash Washing Medium (Active Motif) for 10 min each at RT. Samples were incubated with appropriate secondary antibodies at a concentration of approximately 10 μg/mL together with 300 nM DAPI (when nuclear imaging was required; DAPI was from Thermo Fisher Scientific) in MAXbind Staining Medium for at least 1 h at 37 °C, for 5 μm thick tissue (further optimization of incubation duration or temperature may be needed for thicker tissues), then washed in MAXwash Washing Medium three times for 10 min each at RT. All the primary antibodies used in this work are listed in **Supplementary Table 15**. Secondary antibodies used were: goat anti-chicken Alexa 488 (ThermoFisher Scientific, cat# A-11039), goat anti-rabbit Alexa 546 (ThermoFisher Scientific, cat# A-11010) and goat anti-mouse CF633 (Biotium, cat# 20341); except goat anti-guinea pig Alexa 488 (ThermoFisher Scientific, cat# A-11073) was used in **Supplementary Figure 6**, goat anti-mouse Atto 647N (Sigma-Aldrich, cat# 50185) was used in **Figure 3**, and goat anti-chicken Alexa 546 (ThermoFisher Scientific, cat# A-11040) and goat anti-rabbit Alexa 488 (ThermoFisher Scientific, cat# A-11008) were used in **Figure 4**.

Chemical treatment for protein preservation. The expansion microscopy method used is a variation of our previously reported proExM protocol[9]. Acryloyl-X, s.e.m. (6-((acryloyl)amino)hexanoic acid, succinimidyl ester, here abbreviated AcX, fromThermo Fisher Scientific) was dissolved in anhydrous DMSO at a concentration of 10 mg/mL, then it was aliquotted and stored frozen in a desiccated environment at −20 °C. Tissue slides were incubated with 0.03–0.1 mg/ml AcX (0.03 mg/ml for samples fixed with nonaldehyde fixatives, 0.1 mg/ml for samples fixed with aldehyde fixatives) diluted in PBS buffer for at least 3 h at RT. Note that thicker samples require longer incubation times.

***In situ* polymer synthesis.** The method for *in situ* polymer synthesis in ExPath is slightly modified from our original proExM protocol[8]. Briefly, a monomer solution made of 1× PBS, 2 M NaCl, 8.625% (w/w) sodium acrylate, 2.5% (w/w) acrylamide and 0.10% (w/w) N,N′-methylenebisacrylamide (or BIS for short) (all from Sigma-Aldrich) was prepared and aliquotted and stored at −20 °C before *in situ* polymer synthesis. The slightly lower BIS concentration caused slightly more expansion than previous protocols, at the expense of slightly lower gel sturdiness. The chemicals 4-hydroxy-2,2,6,6-tetramethylpiperidin-1-oxyl (4HT, Sigma-Aldrich) as an inhibitor, tetramethylethylenediamine (TEMED, Sigma-Aldrich) as an accelerator and ammonium persulfate (APS, Sigma-Aldrich) as an initiator were each added sequentially to the monomer solution to prepare the gelling solution (final concentration, 0.01% (w/w) for 4HT and 0.2% (w/w) for both APS and TEMED). Tissue slides were incubated with the monomer solution for 30 min at 4 °C to allow diffusion of monomer solution into the tissues while preventing premature gelation. Then, a gel chamber was constructed by putting a coverslip on top of the tissue, with spacers on either side of the tissue section to prevent compression of tissue. The gel chamber was filled with the fresh gelling solution. Finally, slice samples were incubated for 1.5–2 h at 37 °C in a humidified atmosphere to complete gelation.

Sample digestion and expansion. After gelation, samples were incubated in 8 U/ml proteinase K (New England Biolabs) in a digestion buffer (modified from the original proExM recipe) consisting of 50 mM Tris (pH 8), 25 mM EDTA, 0.5% Triton X-100 and 0.8 M NaCl; and the tissues were incubated for 3 h at 60 °C or until the completion of digestion (i.e., the gelled tissue is detached from the glass slide and becomes transparent, and the gelled tissue remains flat without bending or twisting in the solution). Digested samples were washed once with 1× PBS buffer for 10 min at RT and stained with 300 nM DAPI in PBS buffer for 20 min at RT; then they were washed once with 1× PBS for 10 min at RT. Finally, gels were placed in doubly deionized water at RT for 10 min to expand. This step was repeated three to five times in fresh water until the size of the expanded sample stabilized. To prevent bacterial growth, we sometimes added sodium azide (final concentration 0.002–0.01%) to the water used for expansion. Note that addition of sodium azide may reduce the expansion factor by around 10%.

Structured illumination microscopy pre-expansion imaging. For **Supplementary Figure 3**, HeLa cells (ATCC CCL2) were fixed with 4% paraformaldehyde for 10 min, washed three times for 5 min each with PBS, and permeabilized with 0.1% Triton X-100 for 15 min. Microtubules in fixed HeLa cells were stained with primary antibodies (rabbit anti-α-tubulin, Abcam) in MAXbind Staining Medium (Active Motif) at a concentration of 10 μg/mL for 1–4 h at 37 °C and then washed in MAXwash Washing Medium (Active Motif) three times for 5 min each. Specimens were then incubated with secondary antibodies and 300 nM DAPI in MAXbind Staining Medium for 1–4 h at 37 °C and then washed in PBS three times for 5 min each. These cells were used as a technology test bed, not to make scientific conclusions, so no detailed scientific justification for the choice of cell line is needed. Cells were authenticated and tested for mycoplasma contamination via standard procedures of the ATCC. Unless specifically stated, all the steps were performed at RT.

For **Figure 1f**, a customized 5 μm thickness breast TMA was prepared and stained with primary (rabbit anti-KRT19, chicken anti-vimentin) as well as secondary antibodies and DAPI as described in "Immunostaining." Super-resolution structured illumination microscopy imaging was performed on a Deltavision OMX Blaze (GE Healthcare) SIM microscope with a 100× 1.40 NA (Olympus) oil objective. Stained samples were imaged with SlowFade Gold (Invitrogen) antifade reagent for suppression of photobleaching and refractive index matching for pre-expansion imaging.

Fluorescent microscopy after expansion. Low-magnification images of specimens (**Fig. 1b**,**c**; 'core' images of **Fig. 3**; **Supplementary Figs. 2e–h**,**4** and **5**) were imaged on a Nikon Ti-E epifluorescence microscope with a SPECTRA X light engine (Lumencor) and a 5.5 Zyla sCMOS camera (Andor), controlled by NIS-Elements AR software, with a 4× 0.13 NA air objective or 10× 0.2 NA air objective (Nikon). For **Figures 1k–m**,**2a–j** and **5** and **Supplementary Figures 2a (ii–vi)**,**b(ii**, **iii**, **v**, and **vi)**,**i**,**j**, **6** and **8**, the images were acquired on

the same microscope with a 40× 1.15 NA water-immersion objective (Nikon). The following filter cubes (Semrock, Rochester, New York) were used: DAPI, DAPI-11LP-A-000; Alexa Fluor 488, GFP-1828A-NTE-ZERO; Alexa Fluor 546, FITC/TXRED-2X-B-NTE; Atto 647N or CF 633, Cy5-4040C-000.

All other fluorescence images were taken on an Andor spinning disk (CSU-X1 Yokogawa) confocal system on a Nikon TI-E microscope body with a 40× 1.15 NA water-immersion objective. DAPI was excited with a 405 nm laser and imaged with a 450/50 emission filter. Alexa Fluor 488 was excited with a 488 nm laser and imaged with a 525/40 emission filter. Alexa Fluor 546 was excited with a 561 nm laser and imaged with a 607/36 emission filter. Atto 647N and CF633 were excited with a 640 nm laser and imaged with a 685/40 emission filter.

To prevent the gels from drifting during imaging following expansion, they were placed in glass-bottom six-well plates with all excess liquid removed. If immobilization was needed, liquid low-melt agarose (2% w/w) was pipetted around the gel and allowed to solidify to encase the gels before imaging.

Figures 1g, **2** and **3** (except core images); **Figure 4**; **Supplementary Figure 7** and **Supplementary Figure 9** are maximum intensity projections (MIPs) of 0.25 µm thickness (in pre-ExM distance units). **Figures 1k–m** and **5** and **Supplementary Figure 8** are MIPs of 2 µm thickness.

Bright-field microscopy. Low-magnification images (**Supplementary Fig. 4**) were acquired on a Nikon Ti-E microscope with a DS-Ri2 sCMOS 16mp Color Camera (Nikon) and white LED illuminator with a 4× 0.13 NA air objective or 10× 0.2 NA air objective. High-magnification images of H&E slides (**Figs. 1j** and **5**; **Supplementary Fig. 9**) were acquired on the Panoramic Scan II (3DHistech) with a 40× 0.95 NA air objective (Zeiss).

Autofluorescence analysis. Background was removed from images by subtraction of mean pixel values from blank regions before analysis. For each fluorescent channel, ten regions of interest containing the brightest fluorescent signals and one area containing only autofluorescence signal, as judged by a pathologist's visual inspection, were selected and used to calculate signal-to-background ratios.

Measurement of the expansion factor and **normalization.** We suggest, as we did here, that users acquire low-magnification images of the sample pre-expansion and postexpansion and then take the ratio of these sizes to calculate the expansion factor, which can be used to normalize the physical size of the postexpansion image to that of the pre-expansion state and thus enable 'biological' length units to be used. This normalization process also nulls out the small (<10%) natural sample-to-sample variability of the expansion process.

Measurement error quantification. This section is based on our previously described method[8] for distortion vector field calculation and root-mean-square (RMS) error calculation, with minor modifications. We semiautomated the distortion vector field and RMS error calculation with improved code, eliminating the need for manual selection of control points for the nonlinear registration that leads to the distortion vector field[8]. Given the challenge of finding matching z planes in pre-expansion versus postexpansion states, the same fields of view in multiple z planes were first imaged pre-expansion and postexpansion. To match z planes pre-expansion and postexpansion, scale-invariant feature transform (SIFT) key points[36] were generated for all possible combination of pairs of pre-expansion z planes and postexpansion z projections (note that, since the sample expands along the z axis, one pre-expansion z plane should correspond to one postexpansion z projection from 4–5 z planes). SIFT key points were generated using the VLFeat open-source library[37] and filtered by random sample consensus (RANSAC) with a geometric model that only permits rotation, translation and uniform scaling. The pair of pre-expansion and postexpansion images with the most SIFT key points was used for image registration by rotation, translation and uniform scaling, as well as calculation of expansion factors and distortion vector fields. By subtracting the resulting vectors at any two points, distance measurement errors could easily be sampled, and the RMS error for such measurements was plotted as a function of measurement length from at least three patients.

Expansion immunoFISH. For ExPath samples being processed for immunohistochemistry plus DNA FISH probing, digested gel samples were placed in hybridization buffer made of 1× PBS, 15% ethylene carbonate, 20% dextran sulfate, 600 mM NaCl and 0.2 mg/ml single-stranded salmon sperm DNA at 85 °C for 30 min; then they were mixed with 30 µL of hybridization buffer that contained SureFISH probes 17q12 HER2 and Chr17 CEP (Agilent/Dako) and was preheated at 85 °C for 10 min. The mixtures were then incubated at 45 °C overnight. The next day, samples were washed with stringency wash buffer made of 1× SSC (150 mM NaCl, 15 mM sodium citrate, pH 7.0) and 20% ethylene carbonate at 45 °C for 15 min, followed by washes with 2× SSC at 45 °C three times for 10 min each. Finally, the gel samples were washed with 0.02× SSC multiple times at RT (5 min each) until the expansion was completed.

Computational nuclear atypia analysis. For the task of evaluating nucleus detection and nucleus segmentation, the analyses leading to the tables and figures listed as follows used 31 cases out of the total of 105 cases: **Supplementary Tables 6–8** and **Supplementary Figure 9**. For the task of image classification (see corresponding section below), the tables and figures listed as follows used all 105 cases: **Supplementary Tables 9–12** and **Figure 5c**. We proposed a framework for classification of expanded tissue images into different categories: normal breast, benign breast lesions (UDH and ADH) and noninvasive breast cancer (DCIS). This image classification framework consisted of four components: image preprocessing, nuclei segmentation, feature extraction and image classification. The image preprocessing and nuclei segmentation pipelines are shown in **Figure 5a**.

Image preprocessing. Due to confocal acquisition (see above) of multiple nonoverlapping image tiles, which required stitching to produce a single image, these tiles exhibited background fluorescent signals. During image preprocessing, a rolling-ball algorithm[38] with ball size set to the average nuclei size was applied to remove background noise. After background noise removal, nucleus-to-background contrast was enhanced by adaptive histogram equalization[39]. These enhanced images were then smoothed by a median filter with radius 10.

Nuclei segmentation. The nuclei segmentation procedure consisted of three steps. First, nuclei were segmented using a Poisson-distribution-based minimum error thresholding method[40]. Standard and global thresholding methods are not as efficient as a minimum error threshold method when there is high variability within the nuclei regions and background regions. In order to address this issue, our locally adaptive thresholding algorithm selected the threshold by modelling the image histogram as a mixture of two Poisson models. The threshold value was computed by minimizing the relative entropy between the image histogram and the Poisson mixture model. The initial segmentation of nuclei was then improved by a set of morphological operations that include hole filing and morphological closing to fill holes and to combine small fragments of nuclei into single nuclei as well as morphological opening to remove small non-nucleus regions (e.g., blood vessels, parts of fragmented nuclei and artifacts). This segmentation method may undersegment clusters of nuclei that touch each other. Second, to separate the touching and overlapping nuclei, we used a scale-adaptive multiscale Laplacian of Gaussian (MSLoG) filter[41] to produce local maxima and select seed points for nuclei. For selecting local maxima, constant scale produces imprecise nuclear seed points, since nuclear size varies considerably in early breast neoplasia lesions. In order to address the problem of imprecise nuclear seed points, a scale-adaptive MSLoG filter was applied on a given number of scales, and then local maximum points in the scale-space response were selected as seed points. Last, these seed points were used as markers for the marker-controlled watershed algorithm to separate touching and overlapping nuclei.

Feature extraction. After nuclei segmentation, we extracted morphological, first-order and second-order statistical features for each nucleus. The morphological features included shape and geometrical features, which represent extracted nuclear phenotypic information. The computed morphological features were area, convex area, perimeter, equivalent perimeter, eccentricity, orientation, solidity, extent, compactness, major axis length, minor axis length, elliptical minor and major radius. The first-order statistical features corresponded to the distribution of gray-level values within nuclei. The computed first-order statistical features were mean, median, mean absolute deviation, s.d., interquartile range, skewness and kurtosis. The second-order statistical features corresponded to the textural variation inside nuclei.

doi:10.1038/nbt.3892

We computed two types of second-order statistical features using gray-level Haralick co-occurrence[42] and run-length[43] matrices. The co-occurrence matrix GLCM ($i,j; d,\theta$) is square with dimension Ng, where Ng is the total number of gray levels in the image. The value at the ith column and jth row in the matrix was produced by counting the total number of occasions where a pixel with value i is adjacent to a pixel with value j at a distance d and angle θ. Then the whole matrix was divided by the total number of such comparisons that were made. Alternatively, we can say that each element of the GLCM matrix is considered as the probability that a pixel with gray level i is to be found with a pixel with gray level j at a distance d and angle θ. We defined adjacency in four directions (vertical, horizontal, left and right diagonals) with one displacement vector, which produced four GLCM matrices. In our case, texture information was rotationally invariant. So we took the average in all four directions and produced one GLCM matrix. Later, we computed 14 features proposed by Haralick from the GLCM in order to identify texture more compactly. These 14 features were autocorrelation, correlation, contrast, cluster shade, cluster prominence, energy, entropy, homogeneity, inverse difference normalized, inverse difference moment normalized, dissimilarity, maximum probability, information measure correlation 1 and information measure correlation 2.

The set of consecutive pixels, with the same gray level, collinear in a given direction, constitutes a gray-level run-length matrix GLRLM ($i,j; \theta$). The dimension of the GLRLM is $Ng \times R$, where Ng is the number of gray levels, and R is the maximum run length. Similar to the GLCM, we computed GLRLMs for four directions and averaged them. The 11 run-length features, derived from the GLRLM, are short run emphasis (SRE), long run emphasis (LRE), gray level nonuniformity (GLN), run length nonuniformity (RLN), ratio-percentage (RP), low gray level runs emphasis (LGLRE), high gray level runs emphasis (HGLRE), short run low gray level emphasis (SRLGLE), short run high gray level emphasis (SRHGLE), long run low gray level emphasis (LRLGLE) and long run high gray level emphasis (LRHGLE). In total, we computed 45 features for each nucleus. Last, these features were summarized at the image level by computing the first-order statistics, including mean, median, mean absolute deviation, s.d., interquartile range, skewness and kurtosis of each feature per image, producing 315 summary features per image.

Image classification. In the last part of our framework, we performed logistic regression with Lasso regularization to build multivariate image feature-based models to classify normal, benign and preinvasive malignant tissue images. The analyses were implemented in R (http://www.r-project.org/), using the glmnet package[44]. Lasso regularization[45] was used to create simpler models less prone to overfitting than those that would be obtained from standard logistic regression. The Lasso procedure consists of performing logistic regression with an L1 regularization penalty, which has the effect of shrinking the regression weights of the least predictive features to 0. The amount of the penalty (and the number of nonzero features in the model) is determined by the regularization parameter λ. This method has been shown to perform well in the setting of colinearity[46] and has been widely used to build predictive models from high-dimensional data in translational cancer research. Features were standardized separately in the training and validation data sets before model construction, using the selected setting in glmnet. We evaluated model performance with six-fold cross-validation (6F-CV). For validation, we selected the value of λ that achieved the maximum area under curve (AUC) in cross-validation on the training data set and applied this fixed model to the validation data set. Model performance was assessed by computing the AUC of true positives versus false positives, where a perfect classifier would achieve an AUC of 1, and a random classifier would achieve an AUC of 0.5.

We also evaluated our framework using two other machine learning classifiers, which are commonly used in biomedical research. A Random Forest classifier[47] fits a number of decision trees on various subsamples of the data set and uses averaging to improve the predictive accuracy and to control overfitting. Number of trees (numTrees), maximum depth of the tree (maxDepth) and number of features (numFeatures) to be used in random selection are three parameters that affect the performance of the Random Forest classifer. In our experiments we used numTrees = 100, maxDepth = 30 and numFeatures = 20. The other classifier we explored was Naïve Bayes[48], which is a probabilistic classifier based on applying Bayes' theorem with strong independence assumptions between the features. As the predicted value is class label (i.e., we are pursuing a classification problem), the independence assumption is less restrictive for classification as compared to regression[48].

Image classification results. We applied our image classification framework to images from both pre-expanded and expanded samples. Both data sets consisted of 105 images containing 36 normal breast tissue images, 31 benign lesion breast tissue images (15 UDH and 16 ADH) and 38 noninvasive breast tissue images (DCIS) from 41 cases (likely different patients, but since patients were identified only by sex and age in commercial samples, this is a lower bound). Thus, these 105 images belonged to four different classes (normal, UDH, ADH and DCIS). The ground-truth classification was performed and validated by three certified pathologists and authors of this study (E.-Y.O., V.T. and S.J.S.) from more than 350 examined cases. The total number of images was 131; 105 images were analyzed, and 26 were excluded because they were judged to be borderline diagnostic cases. In order to discriminate normal breast tissue versus benign and noninvasive, we performed binary classification for all classes (**Fig. 5c**). When discriminating normal breast tissue versus UDH, ADH and DCIS tissue, the GLMNET classifier reported AUC values of 0.95, 0.96 and 0.94 for expanded data as compared to AUC values of 0.86, 0.82 and 0.75, respectively, for pre-expanded data. For differentiating nonatypical breast tissue (UDH) from atypical breast tissues (ADH and DCIS), the GLMNET classifier reported AUC values of 0.93 and 0.89 for expanded data as compared to AUC values of 0.71 and 0.82, respectively, for pre-expanded data. For discriminating atypical benign breast tissue (ADH) versus noninvasive breast cancer tissue (DCIS), the GLMNET classifier reported an AUC value of 0.95 for expanded data as compared to an AUC value of 0.84 for pre-expanded data. A comparison of GLMNET classification results versus two other machine learning classifiers (Naïve Bayes and Random Forest) is reported in **Supplementary Table 9**. Top-performing features in expanded and pre-expanded data are reported in **Supplementary Tables 10** and **11**, respectively.

Statistical analysis. Statistical analyses were performed with R (version 3.2.5). Data are presented as mean ± s.d. (SD) or s.e.m. (SEM) with sample numbers n noted in the text, tables and figure legends. Student's t-test was used to determine significant differences between means. A bootstrapped paired t-test was used to statistically compare receiver operator curves. In the boxplot graphs, the ends of whiskers are defined by the s.d., and the central rectangle spans from minimum to maximum; the segment in the rectangle indicates the median, and the square symbol indicates the mean.

Data availability statement. The expansion pathology protocol and the code used for the computational nuclear atypia analysis are posted at http://expansionmicroscopy.org. Data are available upon request to the corresponding authors of the paper.

36. Lowe, D.G. Distinctive image features from scale-invariant keypoints. *Int. J. Comput. Vis.* **60**, 91–110 (2004).
37. Vedaldi, A. & Fulkerson, B. VIfeat - an open and portable library of computer vision algorithms. In *Proc. 18th ACM International Conference on Multimedia* (eds. Bimbo, A.D. *et al.*) 1469–1472 (ACM Press, 2010).
38. Sternberg, S.R. Biomedical image processing. *Computer* **16**, 22–34 (1983).
39. Zuiderveld, K. Contrast limited adaptive histogram equalization. In *Graphics gems IV* (Ed. Heckbert, P.S.), 474–485 (AP Professional, 1994).
40. Fan, J. Notes on Poisson distribution-based minimum error thresholding. *Pattern Recognit. Lett.* **19**, 425–431 (1998).
41. Al-Kofahi, Y., Lassoued, W., Lee, W. & Roysam, B. Improved automatic detection and segmentation of cell nuclei in histopathology images. *IEEE Trans. Biomed. Eng.* **57**, 841–852 (2010).
42. Haralick, R.M., Shanmugam, K. & Dinstein, I. Textural features for image classification. *IEEE Trans. Syst. Man Cybern.* **3**, 610–621 (1973).
43. Galloway, M.M. Texture analysis using gray level run lengths. *Comput. Graph. Image Process.* **4**, 172–179 (1975).
44. Friedman, J., Hastie, T. & Tibshirani, R. Regularization paths for generalized linear models via coordinate descent. *J. Stat. Softw.* **33**, 1–22 (2010).
45. Tibshirani, R. Regression shrinkage and selection via the lasso. *J. R. Stat. Soc. B* **58**, 267–288 (1996).
46. Dormann, C.F. *et al.* Collinearity: a review of methods to deal with it and a simulation study evaluating their performance. *Ecography (Cop.)* **36**, 27–46 (2013).
47. Breiman, L. Random forests. *Mach. Learn.* **45**, 5–32 (2001).
48. John, G.H. & Langley, P. Estimating continuous distributions in Bayesian classifiers. In *Proc. of the 11th Conference on Uncertainty in Artificial Intelligence* (eds. Besnard, P. & Hanks, S.) 338–345 (Morgan Kaufmann Publishers, 1995).

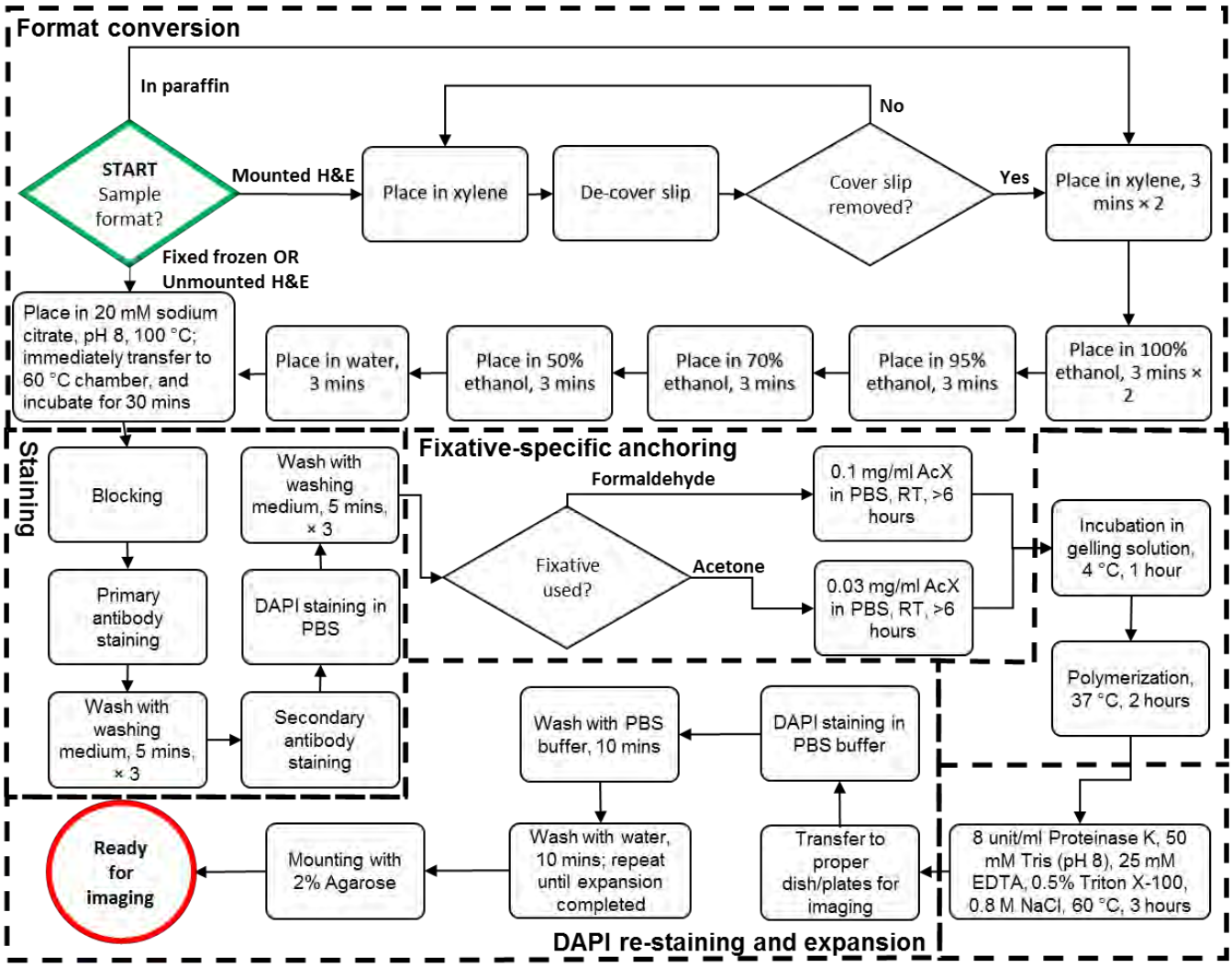

Supplementary Figure 1

The full workflow of Expansion Pathology.

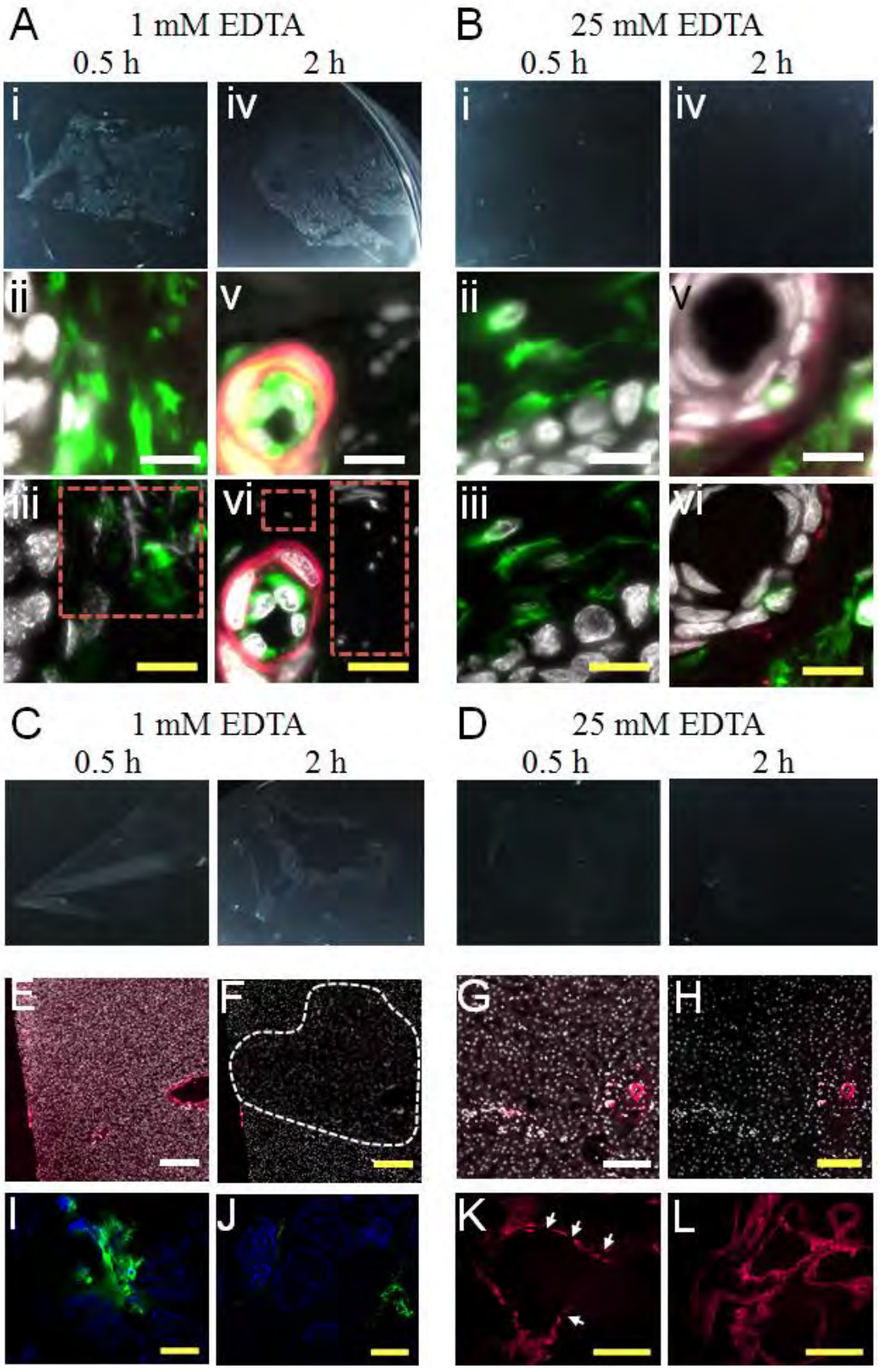

Nature Biotechnology: doi:10.1038/nbt.3892

Supplementary Figure 2

Conditions that affect the successful expansion of human tissues.

(**A**) Images of human skin samples, both taken by a conventional camera (i, iv) and via fluorescence microscopy (**ii-iii, v-vi**) when stained with DAPI (grey) and antibodies against vimentin (green) and smooth muscle actin (gene name, ACTA2) (magenta). The samples were digested with 8 units/mL proteinase K solution containing 25 mM Tris (pH 8), 1 mM EDTA, 0.25% Triton X-100, and 0.4 M NaCl at 60°C for 0.5 hour (**i-iii**) or 2 hours (**iv-vi**). (**i** and **iv**) Conventional camera (i.e., non-fluorescent) photographs of human skin-hydrogel hybrid samples in PBS (~2x expansion), after digestion for 0.5 hour (**i**) or 2 hours (**iv**). (**ii**) Widefield fluorescent image from the sample of (**i**) pre-digestion. (**iii**) Post-expansion wide-field fluorescent image of the sample of (**ii**), with a dashed orange box highlighting regions with autofluorescence in the DAPI channel and distorted vimentin networks post-expansion. (**v**) As in (**ii**), for the sample in (**iv**) pre-digestion. (**vi**) As in (**iii**) for the sample of (**v**) with a dashed orange box highlighting regions with autofluorescence in the DAPI channel. (**B**) As in (**A**), except that the samples were digested with 8 units/mL proteinase K solution containing 25 mM Tris (pH 8), 25 mM EDTA, 0.25% Triton X-100, and 0.4 M NaCl, at 60°C for 0.5 hour (**i-iii**) or 2 hours (**iv-vi**). Note that in **Bi** and **Biv** the samples look quite transparent, due to the heavy digestion. (**C**) Photographs of human liver samples digested with a 1 mM EDTA-based solution – specifically, 8 units/mL proteinase K solution containing 25 mM Tris (pH 8), 1 mM EDTA, 0.25% Triton X-100, and 0.4 M NaCl at 60°C for 0.5 hour (left) or 2 hours (right). (**D**) Photographs of human liver samples digested with a 25 mM EDTA-based solution – specifically, 8 units/mL proteinase K solution containing 25 mM Tris (pH 8), 25 mM EDTA, 0.25% Triton X-100, and 0.4 M NaCl at 60°C for 0.5 hours (left) or 2 hours (right). Note that the samples of **D** are significantly more transparent than those of **C**. (**E)** Widefield fluorescent image of a human liver sample stained with DAPI (grey) and an antibody against smooth muscle actin (gene name, ACTA2) (magenta) prior to the ExPath process. (**F**) Post-expansion wide-field fluorescent image of the sample of **E,** digested with a 1 mM EDTA-based solution for 1 hour. White dashed line outlines an out-of-focus region caused by distortion. (**G**) Wide-field fluorescent image of a human liver sample stained with DAPI (grey) and an antibody against smooth muscle actin (gene name, ACTA2) (magenta) prior to the ExPath process. (**H**) Post-expansion wide-field fluorescent image of the same sample as in **G**. The sample had been digested with a 25 mM EDTA-based solution for 0.5 hour. (**I**) Post-expansion confocal image of human lymph node tissue with invaded breast cancer stained with DAPI (blue) and an antibody against vimentin (green), and treated with a 1 mM EDTA-based solution for 3 hours. (**J**) Post-expansion confocal image of a different sample from the same tissue used in **I**, treated with a 25 mM EDTA-based solution. (**K**) Post-expansion confocal image of normal human kidney tissue fixed with acetone, stained with an antibody against collagen IV (magenta), and treated with 0.1 mg/ml Acryloyl-X prior to *in situ* polymerization. Cracks are indicated by white arrows. (**L**) Post-expansion confocal image of a different sample from the same tissue used in **K**, treated with 0.03 mg/ml Acryloyl-X prior to *in situ* polymerization. Scale bars (yellow scale bars indicate post-expansion images: **Aii** and **iii**, 9.2 μm (physical size in **iii**: 40 μm, expansion factor: 4.33). **Av** and **vi**, 9.4 μm (physical size in **vi**: 40 μm, expansion factor: 4.28). **Bii** and **iii**, 9 μm (physical size in **iii**: 40 μm, expansion factor: 4.41). **Bv** and **vi**, 8.9 μm (physical size in **vi**: 40 μm, expansion factor: 4.51). **E** and **F**, 119 μm (physical size in **F**: 500 μm, expansion factor: 4.22); **G** and **H**, 109 μm (physical size in **H**: 500 μm, expansion factor: 4.58). (**I-L**) 40 μm, physical size.

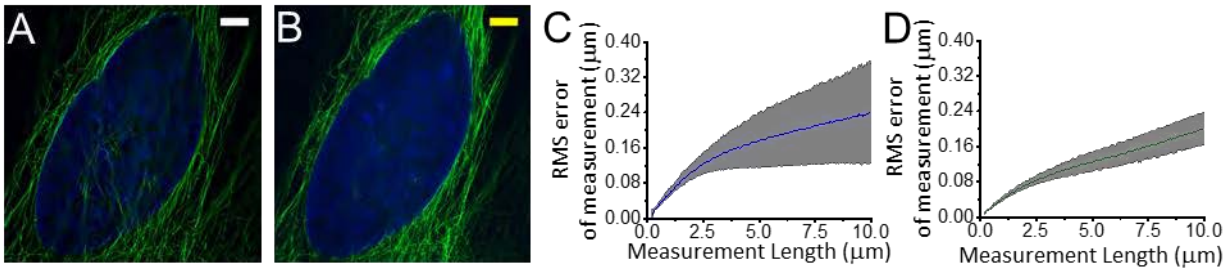

Supplementary Figure 3

Distortion evaluation of post-expansion HeLa cells processed by 25 mM EDTA-assisted proteinase K digestion.

(**A**) Super-resolution structured illumination microscopy (SR-SIM) image of a HeLa cell stained with DAPI and an antibody against α-tubulin. Blue, DAPI; green, α-tubulin. (**B**) Post-expansion image of the same sample acquired with a spinning disk confocal microscope. (**C** and **D**) Root mean square (RMS) length measurement error as a function of measurement length for ExPath vs SIM images (blue solid line, mean of DAPI channel; green solid line, mean of α-tubulin channel; shaded area, standard deviation; n = 3 samples from separate cultures). Scale bars: (**A**) 4 μm, (**B**) 4 μm (for yellow scale bar, physical size post-expansion, 19.5 μm; expansion factor: 4.89).

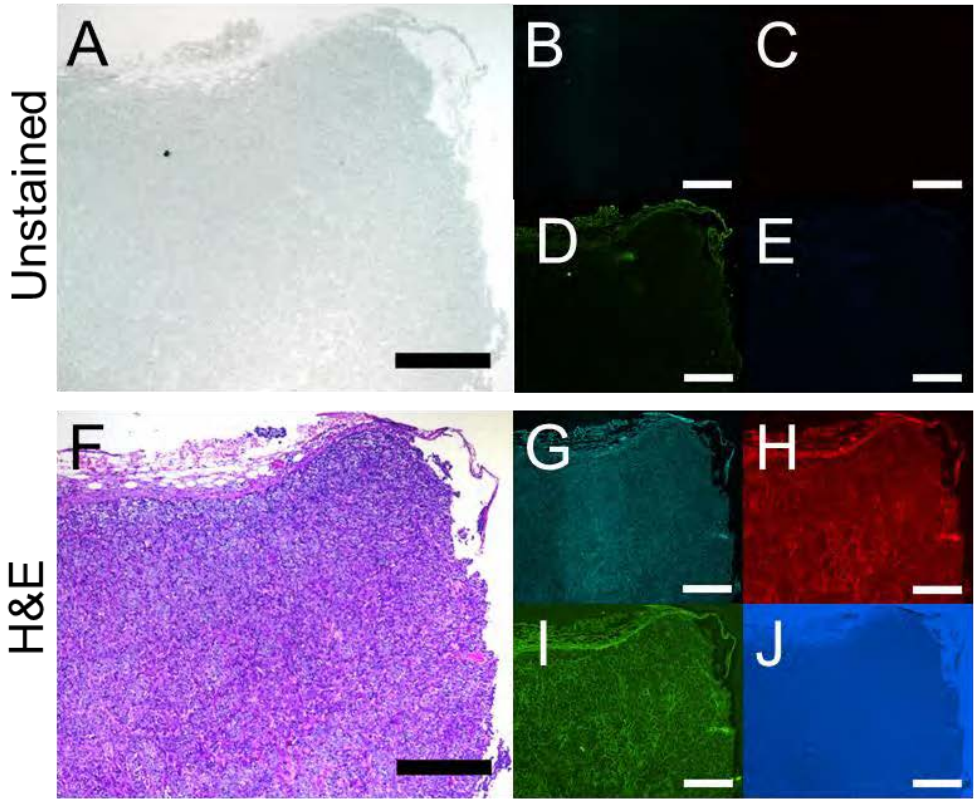

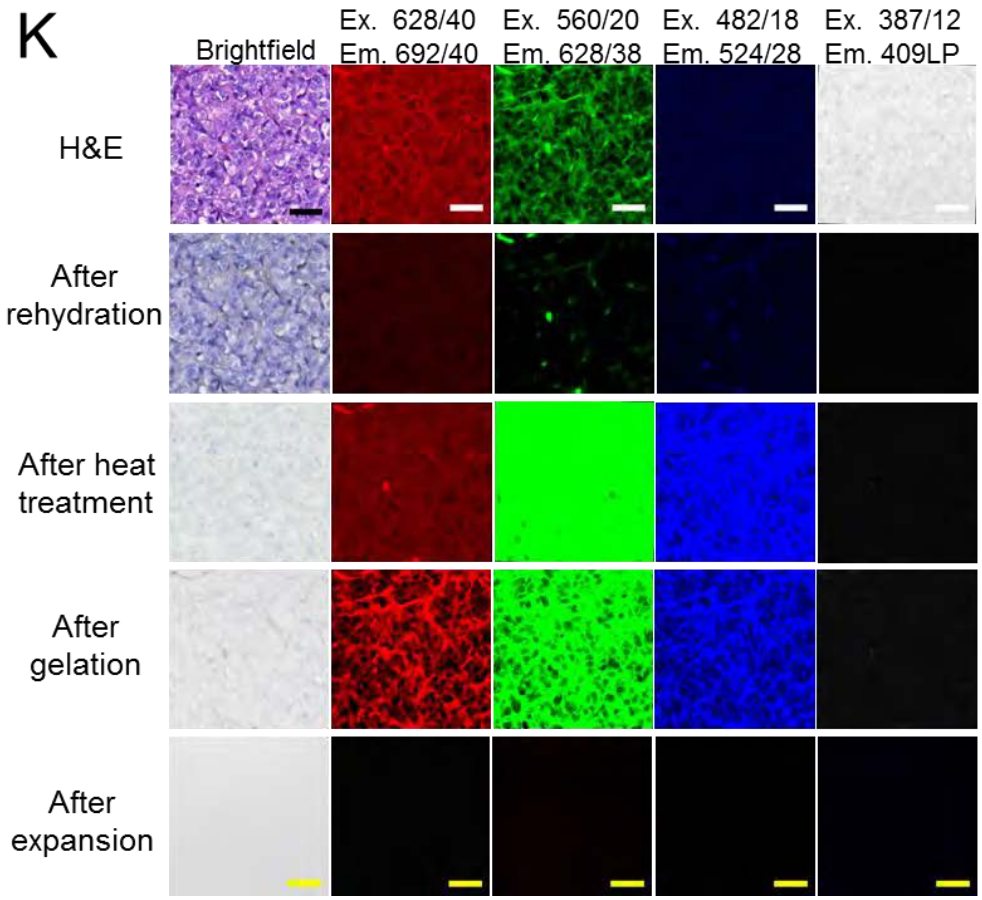

Nature Biotechnology: doi:10.1038/nbt.3892

Supplementary Figure 4

Fluorescence of unstained tissue vs. H&E stained tissue.

(A) Brightfield image of unstained formalin-preserved human lymph node tissue with invaded breast cancer. (**B-E**) Widefield fluorescent images of the same sample as in **A** in four fluorescent channels (listed below). (**F**) Bright field image of tissue from the same block as in **A**, stained with H&E. (**G-J**) Widefield fluorescent images of the sample of **F** in four fluorescent channels. Filters for each fluorescent channel (Semrock, Rochester, NY): **B** and **G**: excitation 628 ± 20 nm, emission 692 ± 20 nm; **C** and **H**: excitation 586 ± 10 nm, emission 628 ± 19 nm; **D** and **I**: excitation 482 ± 9 nm, emission 520 ± 14 nm; **E** and **J**: excitation 387 ± 6 nm, emission 409 nm and longer. Images from a given fluorescent channel are adjusted to have the same contrast. (**K**) Brightfield and widefield fluorescent images of tissue from the same block as in **A**, stained with H&E, after each step of ExPath processing. Images from a given fluorescent channel are adjusted to have the same contrast. Samples may be especially bright after the heat treatment and gelation steps due to the buffer compositions present. Scale bars: **A-J**, 500 μm; **K**, 40 μm (for yellow scalebars, post-expansion, physical size 184 μm; expansion factor: 4.58).

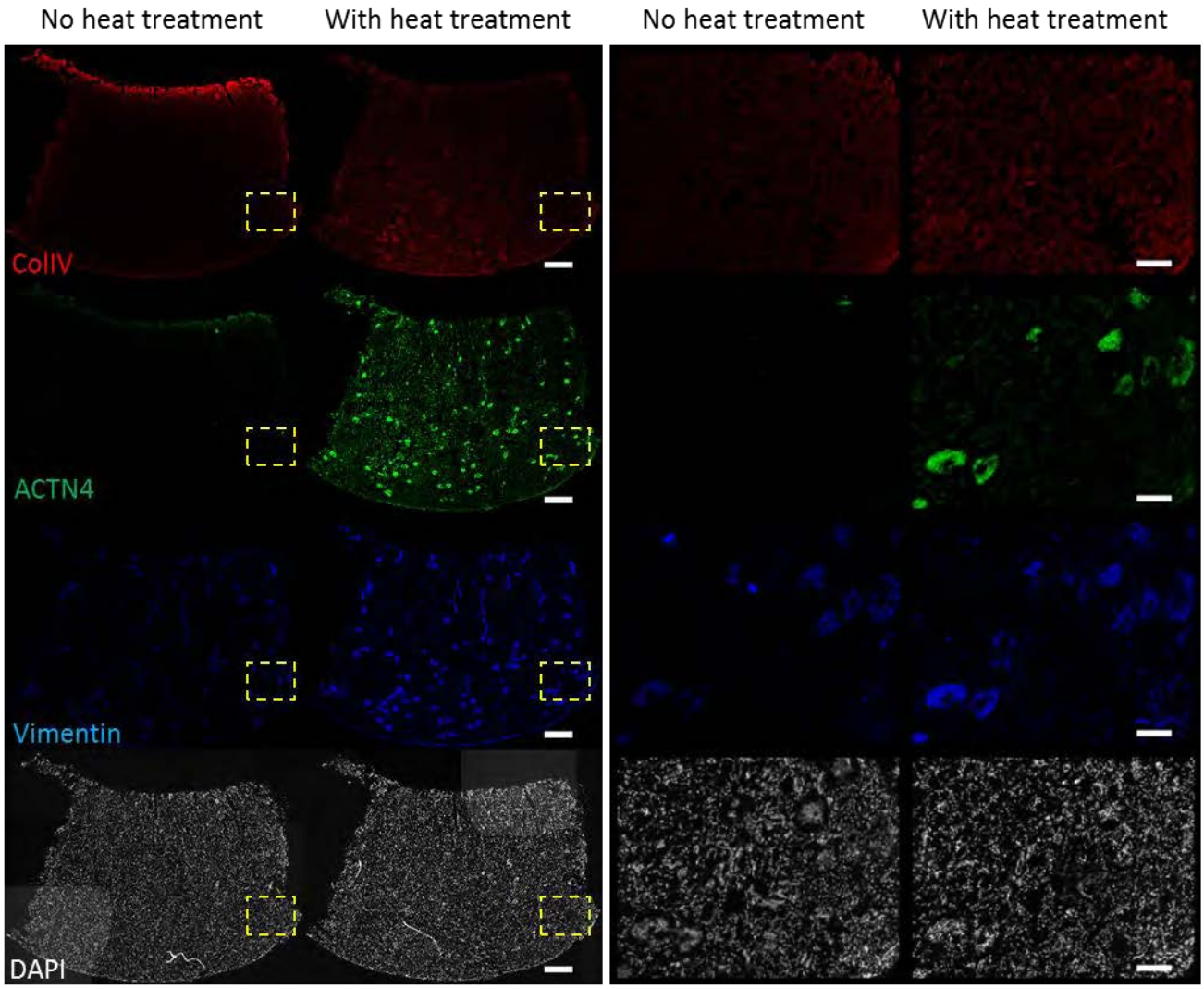

Supplementary Figure 5

Heat treatment significantly improves immunostaining of vimentin and actinin-4 on human kidney samples.

Left panel, widefield fluorescent images of acetone fixed human kidney sections with and without heat treatment in citrate buffer. Right panel, zooms into regions corresponding to the regions indicated by the dashed yellow rectangles in the left panels. Scale bars: 1 mm (left panel), 200 µm (right panel). Abbreviations: ACTN4, actinin-4; ColIV, collagen IV.

Nature Biotechnology: doi:10.1038/nbt.3892

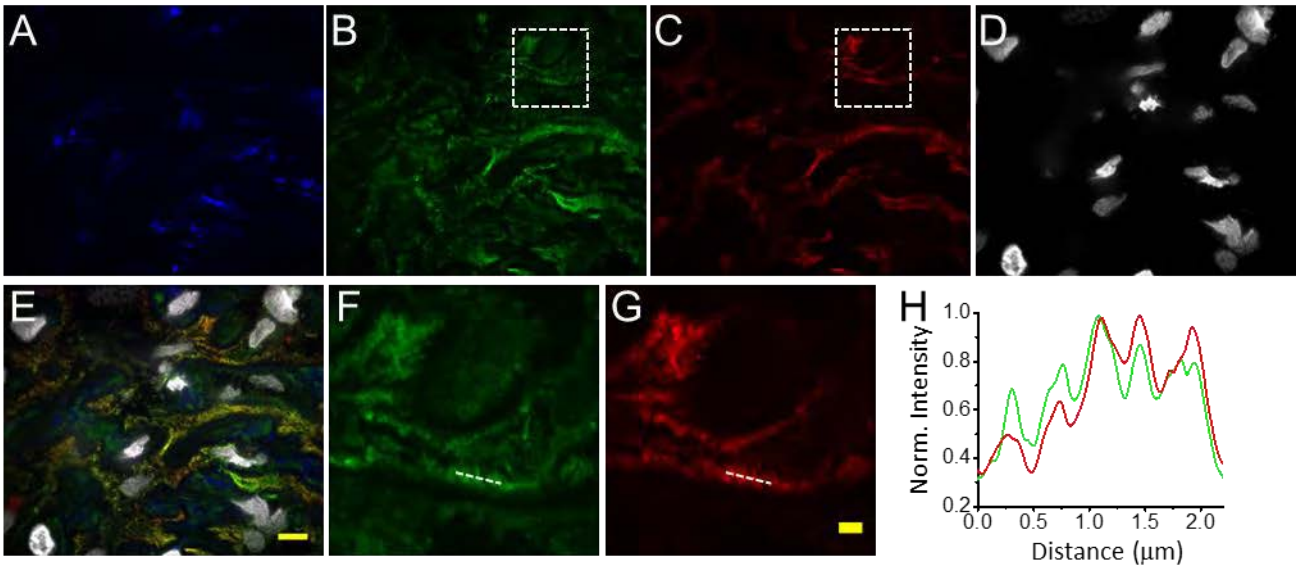

Supplementary Figure 6

Anti-actinin-4 specifically stains tertiary podocyte foot processes.

(**A-D**) Post-expansion widefield images of a human acetone fixed kidney section stained with DAPI and antibodies. Blue, vimentin; green, actinin-4; red, synaptopodin; grey, DAPI. (**E**) Merged image of (**A-D**). (**F** and **G**) Magnified regions showing actinin-4 (**F**) and synaptopodin (**G**) zoomed into the white dashed squares of **B** and **C**. (**H**) Profiles of fluorescent intensity taken along the white dashed line cuts of **F** and **G**. Green, actinin-4; red, synaptopodin. Scale bars: 1 µm (4.5 µm physical size, expansion factor 4.5).

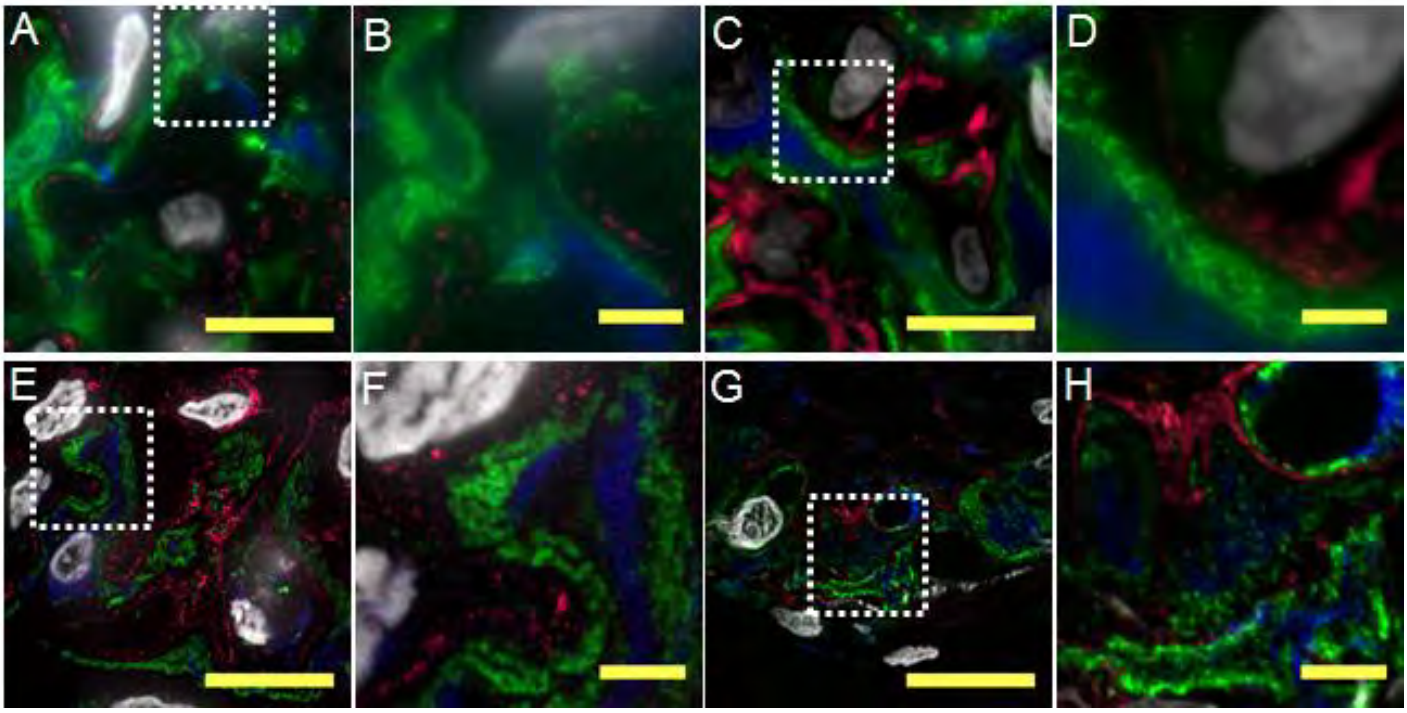

Supplementary Figure 7

Immunostaining images of FFPE kidney samples

A. Post-expansion widefield image of a FFPE normal human kidney sample treated with a citrate antigen retrieval method (20 mM sodium citrate, pH 8.0), with highlighted region (boxed line) magnified in panel **B**. **C**. Post-expansion widefield image of a FFPE normal human kidney sample treated with a Tris-EDTA antigen retrieval method (10 mM Tris base, 1 mM EDTA solution, 0.05% Tween 20, pH 9.0), with highlighted region (boxed line) magnified in panel **D**. **E.** Post-expansion confocal image of a FFPE normal human kidney sample treated with a citrate antigen retrieval method, with highlighted region (boxed line) magnified in **F. G**. Post-expansion confocal image of a FFPE human kidney sample with minimal change disease treated with a citrate antigen retrieval method, with highlighted region (boxed line) magnified in **H**. All the samples were stained with DAPI (gray) and antibodies against vimentin (blue), actinin-4 (green) and collagen IV (magenta). Scale bars: **A**, **C**, **E** and **G,** 40 μm (physical size). **B**, **D**, **F**, and **H**, 8 μm (physical size).

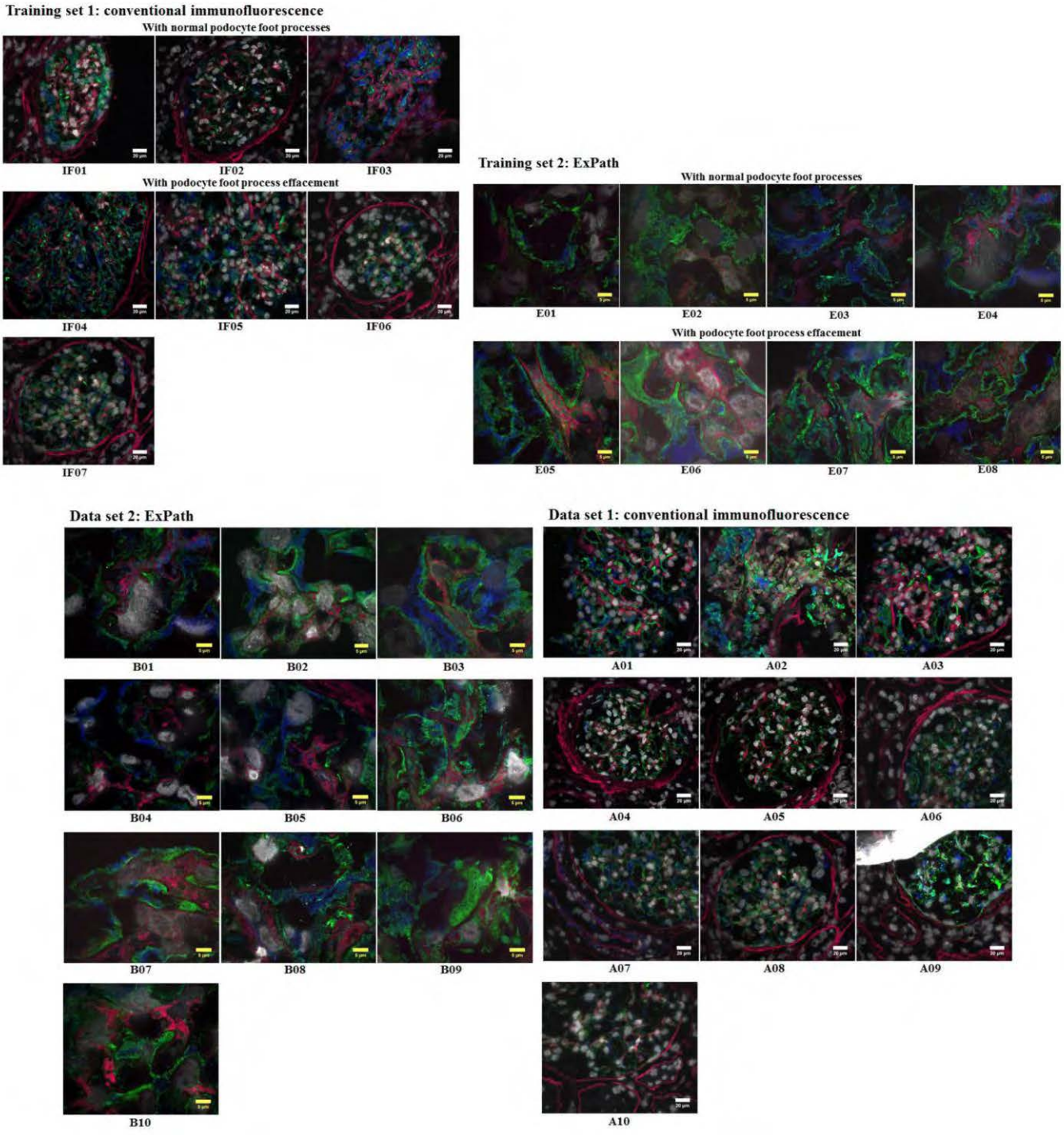

Supplementary Figure 8

Training and and test images for single-blinded nephrotic kidney disease diagnosis.

Frozen kidney sections fixed with acetone were stained with DAPI and antibodies. Blue, vimentin; green, actinin-4; magenta, collagen IV; grey, DAPI. Scale bars are indicated in images. For ExPath images, only physical size is indicated. Expansion factors are listed in **Supplementary Table 4.**

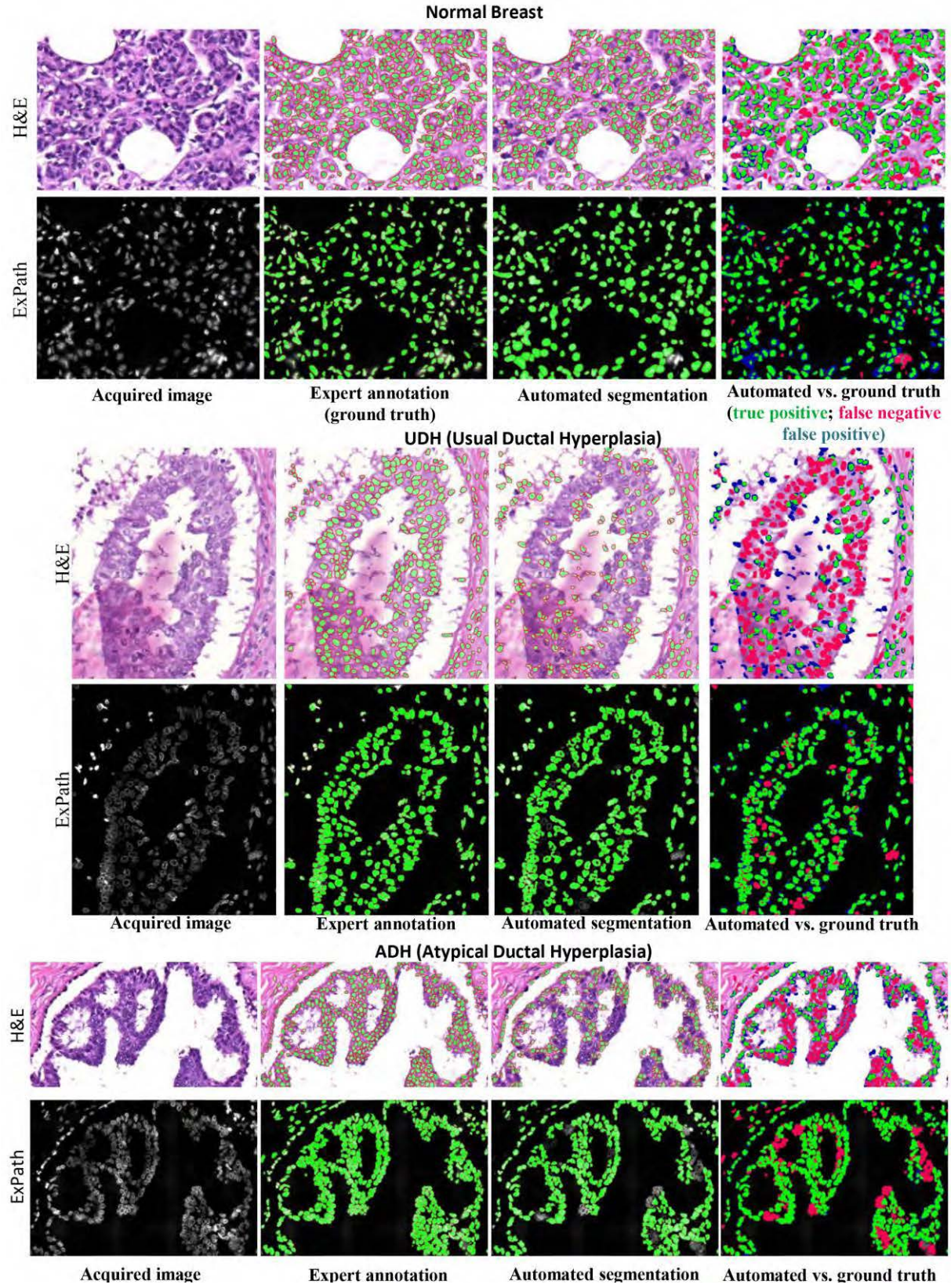

Nature Biotechnology: doi:10.1038/nbt.3892

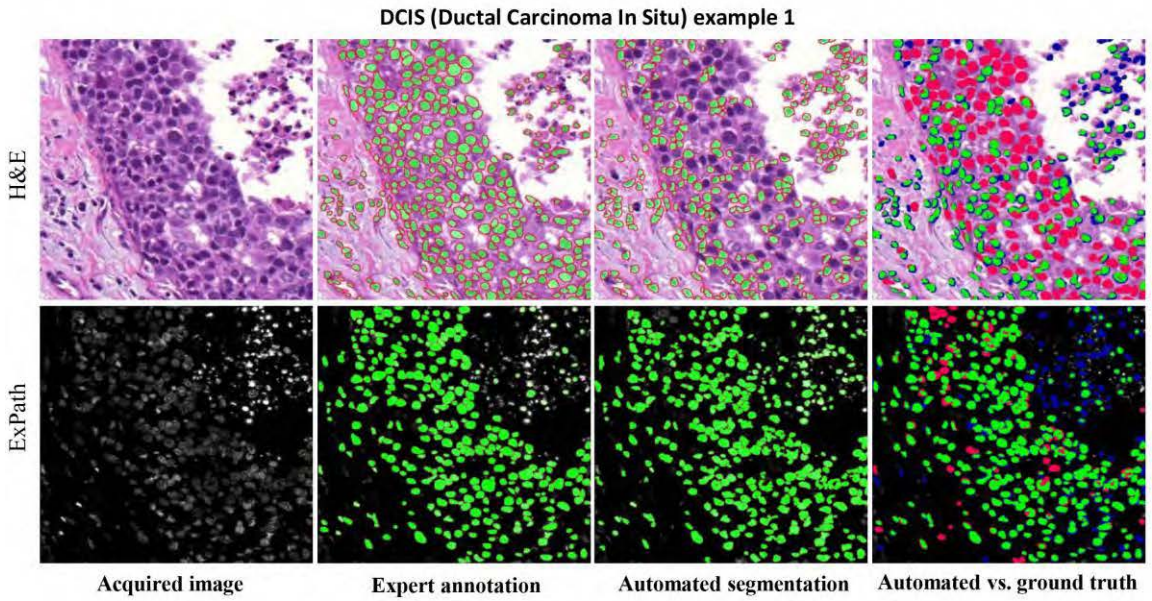

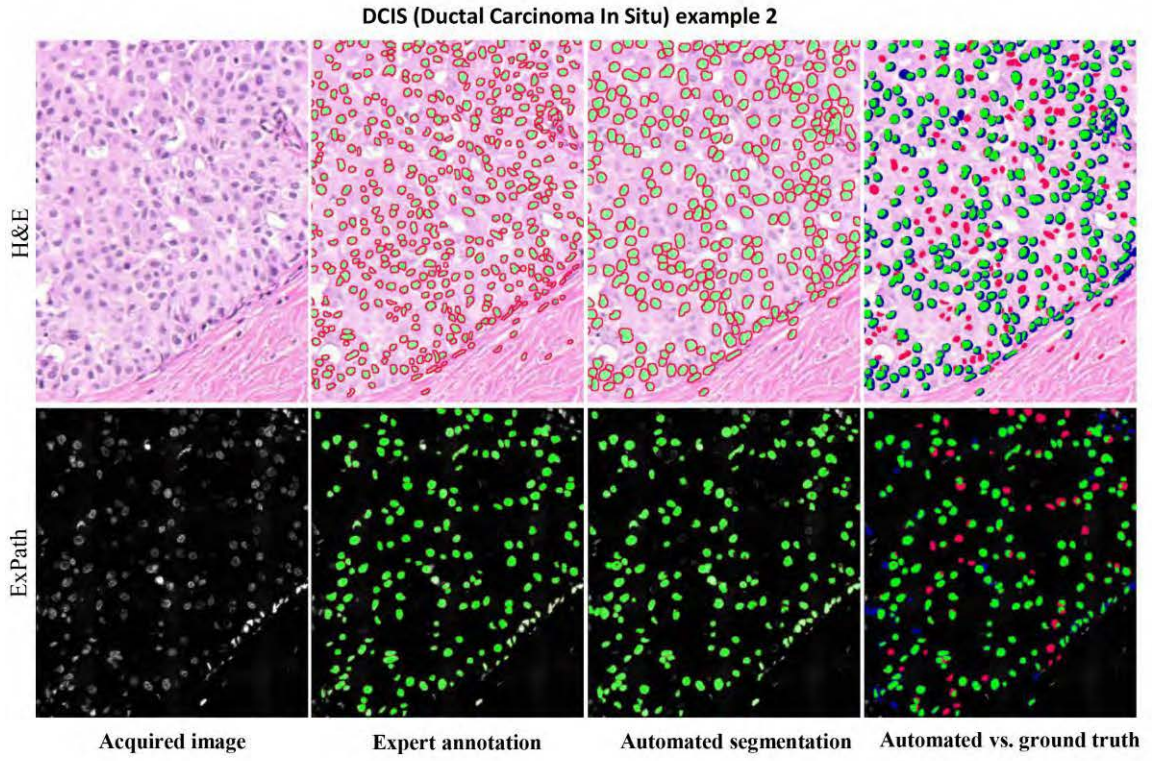

Supplementary Figure 9

Nature Biotechnology: doi:10.1038/nbt.3892

Examples of computational detection and segmentation of the nuclei in pre-expansion H&E images and post-expansion fluorescent images (ExPath).

Computational detection and segmentation of the nuclei is significantly more accurate in expanded samples as compared to pre-expanded samples: examples of normal breast, usual ductal hyperplasia (UDH), atypical ductal hyperplasia (ADH) and ductal carcinoma in situ (DCIS). For the “expert annotation” and “automated segmentation” columns: green filled nuclei are nuclei segmented by the expert or the automated segmentation algorithm, respectively (red circles indicate nucleus outlines, which are not visible in the ExPath row because the resolution is too high and thus the outline is barely visible). In the “automated vs expert” column: green filled nuclei, true positives; red filled nuclei, false negatives; blue filled nuclei, false positives (note that when the automated segmentation yielded larger outlines than the expert, this is expressed as a blue “halo” around the green).

Expansion Pathology

Yongxin Zhao[+1], Octavian Bucur[+2,3,4,5], Humayun Irshad[2,3,5], Fei Chen[1,6,7], Astrid Weins[8,9], Andreea L. Stancu[2,5], Eun-Young Oh[2], Marcello DiStasio[2], Vanda Torous[2], Benjamin Glass[2], Isaac E. Stillman[2], Stuart J. Schnitt[2], Andrew H. Beck[2,3,5*], Edward S. Boyden[1,6,7,10*]

[1]MIT Media Lab, Massachusetts Institute of Technology, Cambridge, MA, USA

[2]Department of Pathology and Cancer Research Institute, Beth Israel Deaconess Medical Center, Harvard Medical School, Boston, MA, USA

[3]Ludwig Center at Harvard Medical School, Boston, MA, USA

[4]Institute of Biochemistry of the Romanian Academy, Bucharest, Romania

[5]Broad Institute of MIT and Harvard, Cambridge, MA, USA

[6]Department of Biological Engineering, Massachusetts Institute of Technology, Cambridge, MA, USA

[7]McGovern Institute, Massachusetts Institute of Technology, Cambridge, MA, USA

[8]Department of Pathology, Brigham and Women's Hospital, Harvard Medical School, Boston, MA, USA

[9]Department of Medicine/Renal Division, Brigham and Women's Hospital, Harvard Medical School, Boston, MA, USA

[10]Department of Brain and Cognitive Sciences, Massachusetts Institute of Technology, Cambridge, MA, USA

[+] made equal contributions.

*correspondence to andy.beck@pathai.com (pathological aspects) and esb@media.mit.edu (technical aspects)

Nature Biotechnology: doi:10.1038/nbt.3892

Supplementary information

Supplementary Note

Supplementary Table 1. The effects of EDTA concentration on proteinase K digestion of human tissue/hydrogel composites.

Supplementary Table 2. The effects of EDTA concentration on proteinase K digestion of human tissue/hydrogel composites, as a function of digestion time.

Supplementary Table 3. Expansion factors for samples in **Figure 3**.

Supplementary Table 4. Information about images used in **Supplementary Figure 8**.

Supplementary Table 5. Observations on samples in **Supplementary Figure 8** made by observers.

Supplementary Table 6. ExPath improves automated nucleus detection and segmentation in expanded breast neoplasia specimens.

Supplementary Table 7. ExPath improves nucleus detection in all breast tissue types, as well as on clearly visible and dim nuclei.

Supplementary Table 8. ExPath improves nucleus segmentation in all breast tissue types, as well as on clearly visible and dim nuclei.

Supplementary Table 9. Binary-classification results (AUC ROC) with three different state of the art classifiers (Naïve Bayes, Random Forest and GLMNET).

Supplementary Table 10. List of top-performing features for building classification models for ExPath.

Supplementary Table 11. List of top-performing features for building classification models for pre-expansion data.

Supplementary Table 12. Binary-classification results (AUC ROC; GLMNET) with or without using normalized expansion factors.

Supplementary Table 13. Comparison of technical capabilities of the current version of ExPath vs. electron microscopy.

Supplementary Table 14. Human samples purchased from commercial sources.

Supplementary Table 15. Primary antibodies used.

Supplementary References.

Supplementary Note

The effect of EDTA concentration on tissue digestion. We note that high concentrations of EDTA (>5 mM) are often used for enzyme-free, live-cell tissue dissociation in preparation for flow cytometry[1,2]. For our fixed tissue experiments, we used 25 mM EDTA to facilitate more effective proteinase K (ProK) digestion. We examined the effects of EDTA at 1 mM vs. 25 mM concentration in the digestion of human samples including skin, liver, breast and lung, including acetone-fixed as well as FFPE samples (**Supplementary Fig. 2; Supplementary Tables 1-2**). We also investigated the effect of digestion time under both conditions for human skin and liver FFPE samples (which contain distinct extracellular matrix components and exhibit strong autofluorescence in the blue and green channels (**Supplementary Fig. 2**), most likely due to formalin-fixed extracellular matrix (ECM) proteins[3–5]). We found that both human skin and liver samples were completely digested and fully expanded in <0.5 hours with 25 mM EDTA-assisted proteinase K digestion. On the other hand, the ECM was not fully digested in either type of tissue with 1 mM EDTA as suggested by residual autofluorescence (**Supplementary Figs. 2Aiii and Avi**). Incomplete digestion can cause distortions at both micro- and macro- scales. For many other types of tissue, either low or high EDTA will work (**Supplementary Tables 1-2**). Our results suggest that 25 mM EDTA is preferred for the digestion step, and digestion time could be as short as 0.5 hours for 50-μm-thick or thinner human FFPE tissue specimens.

Supplementary Tables

Supplementary Table 1. The effects of EDTA concentration on proteinase K digestion of human tissue/hydrogel composites.

	Digestion* with 1 mM EDTA		Digestion with 25 mM EDTA	
	Fresh Frozen	FFPE	Fresh Frozen	FFPE
Skin	✓	✗	✓	✓
Liver	✓	✗	✓	✓
Lung	✓	✓	✓	✓
Breast	✓	✗	✓	✓

*Digestion condition: 8 units/mL proteinase K solution containing 25 mM Tris (pH 8), 0.25% Triton X-100, 0.4 M NaCl, in 60 °C for 3 hours.

✓ Complete digestion.

✗ Incomplete digestion.

Supplementary Table 2. The effects of EDTA concentration on proteinase K digestion of human tissue/hydrogel composites, as a function of digestion time.

Human tissue type	**EDTA concentration**	**Digestion time**			
		0.5 h	**1 h**	**1.5 h**	**2 h**
Skin	**1 mM**	✗	✗	✗	✗
	25 mM	✓	✓	✓	✓
Liver	**1 mM**	✗	✗	✗	✗
	25 mM	✓	✓	✓	✓

Supplementary Table 3. Expansion factors for samples in **Figure 3**.

Human organ	**Size of yellow scale bar in biological units, in post-expansion images, in µm (with expansion factor*)**			
	Normal		**Cancer**	
	Top (physical scalebar size, 50 µm)	**Bottom** (physical scalebar size, 12.5 µm)	**Top** (physical scalebar size, 50 µm)	**Bottom** (physical scalebar size, 12.5 µm)
Prostate	10.4 (4.8x)	2.6 (4.8x)	10.2 (4.9x)	2.5 (4.9x)
Lung	10.4 (4.8x)	2.6 (4.8x)	11.11 (4.5x)	2.8 (4.5x)
Breast	12.5 (4.0x)	3.1 (4.0x)	10.6 (4.7x)	2.7 (4.7x)
Pancreas	10.4 (4.8x)	2.6 (4.8x)	10 (5.0x)	2.5 (5.0x)

Nature Biotechnology: doi:10.1038/nbt.3892

Ovary	10.2 (4.9x)	2.5 (4.9x)	10.6 (4.7x)	2.7 (4.7x)
Liver	10.6 (4.7x)	2.7 (4.7x)	10.4 (4.8x)	2.6 (4.8x)
Kidney	10.4 (4.8x)	2.6 (4.8x)	10.6 (4.7x)	2.7 (4.7x)
Colon	10.6 (4.7x)	2.7 (4.7x)	10.4 (4.8x)	2.6 (4.8x)

*Average expansion factor: 4.7 (standard deviation: 0.2).

Supplementary Table 4. Information about images used in **Supplementary Figure 8**.

Image ID (as used in Supp. Fig. 8)	Case #	State	FPE?	Expanded?	Expansion factor
IF01	1	Normal	No	No	-
IF02	2	Normal	No	No	-
IF03	3	Normal	No	No	-
IF04	4	MCD	Yes	No	-
IF05	5	MCD	Yes	No	-
IF06	6	MCD	Yes	No	-
IF07	7	FSGS	Yes	No	-
E01	3	Normal	No	Yes	4.3
E02	1	Normal	No	Yes	4.4
E03	2	Normal	No	Yes	4.2
E04	8	Normal	No	Yes	4.4
E05	6	MCD	Yes	Yes	4.2
E06	5	MCD	Yes	Yes	4.3
E07	9	MCD	Yes	Yes	4.5
E08	7	FSGS	Yes	Yes	3.8
A01	5	MCD	Yes	No	-
A02	3	Normal	No	No	-
A03	5	MCD	Yes	No	-
A04	2	Normal	No	No	-
A05	2	Normal	No	No	-
A06	6	MCD	Yes	No	-
A07	6	MCD	Yes	No	-
A08	7	FSGS	Yes	No	-
A09	8	Normal	No	No	-
A10	8	Normal	No	No	-
B01	8	Normal	No	Yes	4.4
B02	7	FSGS	Yes	Yes	3.8
B03	6	MCD	Yes	Yes	4.2
B04	2	Normal	No	Yes	4.2
B05	1	Normal	No	Yes	4.4
B06	9	MCD	Yes	Yes	4.5

B07	5	MCD	Yes	Yes	4.3
B08	3	Normal	No	Yes	4.3
B09	5	MCD	Yes	Yes	4.3
B10	8	Normal	No	Yes	4.4

Abbreviation: FPE=foot process effacement; MCD=Minimal Change Disease; FSGS=Focal Segmental Glomerulosclerosis;
Average expansion factor of B and E series: 4.3 (standard deviation 0.2).

Supplementary Table 5. Observation on samples in **Supplementary Figure 8** made by observers.

Image ID (as used in Supp. Fig. 8)	**FPE*?**	**Expanded?**	**Observation made by observers**							
			1	**2**	**3**	**4**	**5**	**6**	**7**	**Fraction correct**
Pre-Expansion										
A01	Yes	No	Yes	Yes	Yes	Yes	Yes	No	No	71.4%
A02	No	No	No	Yes	No	Yes	Yes	Yes	Yes	28.6%
A03	Yes	No	Yes	No	Yes	No	Yes	No	Yes	57.1%
A04	No	No	Yes	Yes	No	Yes	Yes	No	No	42.9%
A05	No	No	No	No	No	No	No	No	No	100.0%
A06	Yes	No	No	No	No	No	No	No	Yes	14.3%
A07	Yes	No	Yes	Yes	Yes	No	Yes	Yes	Yes	85.7%
A08	Yes	No	Yes	Yes	Yes	Yes	Yes	Yes	Yes	100.0%
A09	No	No	Yes	No	No	Yes	No	Yes	No	57.1%
A10	No	No	No	No	No	No	No	No	No	100.0%
Accuracy			70%	60%	90%	40%	70%	50%	80%	**65.7%**
Post-expansion										
B01	No	Yes	No	No	No	No	No	No	No	100.0%
B02	Yes	Yes	Yes	Yes	Yes	Yes	Yes	Yes	Yes	100.0%
B03	Yes	Yes	Yes	Yes	Yes	Yes	Yes	Yes	Yes	100.0%
B04	No	Yes	Yes	Yes	No	Yes	No	No	No	57.1%
B05	No	Yes	No	No	No	No	No	No	No	100.0%
B06	Yes	Yes	Yes	Yes	Yes	Yes	Yes	Yes	Yes	100.0%
B07	Yes	Yes	Yes	Yes	Yes	Yes	Yes	Yes	Yes	100.0%
B08	No	Yes	No	No	No	No	Yes	No	Yes	71.4%
B09	Yes	Yes	Yes	Yes	Yes	Yes	Yes	Yes	Yes	100.0%
B10	No	Yes	No	No	No	Yes	No	No	Yes	71.4%
Accuracy			90%	90%	100%	80%	90%	100%	80%	**90.0%**

*FPE: Foot process effacement.

*Observers were two kidney pathologists, one non-kidney pathologist, one pathology resident, two MDs and one non-MD researcher.

Supplementary Table 6. ExPath improves automated nucleus detection and segmentation in expanded breast neoplasia specimens.

	Nucleus Detection							Nucleus Segmentation			
	Total	**TP**	**FN**	**FP**	**TPR**	**PPV**	**F-Score**	**F-Score**	**Accuracy**	**Kappa**	**GCE**
Pre-Exp	9416	5178	4238	1768	0.56 ±0.14	0.76 ±0.17	0.63 ±0.13	0.64 ±0.17	0.78 ±0.06	0.39 ±0.12	0.30 ±0.08
ExPath	**8649**	**5202**	**3447**	**438**	**0.62 ±0.13**	**0.93 ±0.06**	**0.73 ±0.1**	**0.73 ±0.18**	**0.90 ±0.04**	**0.69 ±0.08**	**0.18 ±0.07**

Abbreviations: TP=true positive; FN=false negative; FP=false positive; TPR=true positive rate; PPV = positive predictive value; Kappa=Cohen kappa coefficient; GCE=global consistency error[6]. For the latter scores, shown is mean ± standard deviation; N = 31 fields of view from 12 patients.

Supplementary Table 7. ExPath improves nucleus detection in all breast tissue types, as well as on clearly visible and dim nuclei.

		Total	**TP**	**FN**	**FP**	**TPR**	**PPV**	**F-Score**
All Nuclei	**Pre-Exp**	9416	5178	4238	1768	0.56 ± 0.14	0.76 ± 0.17	0.63 ± 0.13
	ExPath	8649	5202	3447	438	0.62 ± 0.13	0.93 ± 0.06	0.73 ± 0.1
Clearly Visible Nuclei	**Pre-Exp**	5069	3262	1807	-	0.66 ± 0.18	-	-
	ExPath	4925	3476	1449	-	0.74 ± 0.14	-	-
Dim Nuclei	**Pre-Exp**	4347	1981	2366	-	0.44 ± 0.18	-	-
	ExPath	3597	1899	1698	-	0.65 ± 0.09	-	-

Abbreviations: TP=true positive; FN=false negative; FP=false positive; TPR=true positive rate; PPV = positive predictive value[6]. For the latter scores, shown is mean ± standard deviation; N = 31 fields of view from 12 patients.

Supplementary Table 8. ExPath improves nucleus segmentation in all breast tissue types, as well as on clearly visible and dim nuclei.

		Overlap based Metrics				**Pair-Counting based Metrics**	**Probabilistic Metrics**	
		F-Score	**Accuracy**	**Overlap**	**GCE**	**RI**	**Kappa**	**AUC**
All Nuclei	**Pre-Exp**	0.64 ± 0.17	0.78 ± 0.06	0.49 ± 0.17	0.30 ± 0.08	0.67 ± 0.06	0.39 ± 0.12	0.69 ± 0.07

Clearly Visible Nuclei	**ExPath**	0.73 ± 0.18	0.90 ± 0.04	0.60 ± 0.21	0.18 ± 0.07	0.79 ± 0.07	0.69 ± 0.08	0.85 ± 0.04
	Pre-Exp	0.65 ± 0.16	0.82 ± 0.04	0.50 ± 0.16	0.28 ± 0.06	0.71 ± 0.05	0.43 ± 0.14	0.71 ± 0.10
Dim Nuclei	**ExPath**	0.74 ± 0.17	0.91 ± 0.05	0.61 ± 0.20	0.11 ± 0.07	0.82 ± 0.08	0.74 ± 0.16	0.86 ± 0.06
	Pre-Exp	0.61 ± 0.19	0.77 ± 0.06	0.47 ± 0.18	0.32 ± 0.08	0.65 ± 0.07	0.35 ± 0.12	0.60 ± 0.07
	ExPath	0.70 ± 0.19	0.82 ± 0.06	0.57 ± 0.21	0.25 ± 0.08	0.72 ± 0.08	0.58 ± 0.15	0.73 ± 0.08

Abbreviations: GCE=global consistency error; RI=rand index; Kappa=Cohen kappa coefficient; AUC=area under the curve (receiver operating characteristic curve, a plot of true positive rate against false positive rate)[6]. Mean ± standard deviation; N = 31 fields of view from 12 patients.

Supplementary Table 9. Binary-classification results (AUC ROC) with three different state of the art classifiers (Naïve Bayes, Random Forest and GLMNET).

	Naïve Bayes		**Random Forest**		**GLMNET**		**Combined Results**	
	Pre-Exp	**ExPath**	**Pre-Exp**	**ExPath**	**Pre-Exp**	**ExPath**	**Pre-Exp**	**ExPath**
Normal vs UDH	0.66	**0.81**	0.87	**0.98**	0.86	**0.95**	0.80 ± 0.10	**0.91 ± 0.07**
Normal vs ADH	0.84	0.74	0.78	**0.89**	0.82	**0.96**	0.81 ± 0.02	**0.86 ± 0.09**
Normal vs DCIS	0.77	**0.74**	0.84	**0.87**	0.75	**0.94**	0.79 ± 0.04	**0.85 ± 0.08**
UDH vs ADH	0.81	**0.84**	0.77	**0.94**	0.71	**0.93**	0.76 ± 0.04	**0.90 ± 0.04**
UDH vs DCIS	0.75	**0.90**	0.89	**0.98**	0.82	**0.89**	0.82 ± 0.06	**0.92 ± 0.04**
ADH vs DCIS	0.75	**0.77**	0.79	**0.91**	0.84	**0.95**	0.79 ± 0.04	**0.88 ± 0.08**

Abbreviations: UDH=Usual Ductal Hyperplasia; ADH=Atypical Ductal Hyperplasia; DCIS=Ductal Carcinoma In Situ; mean ± standard deviation; N=3 classification methods.

Supplementary Table 10. List of top-performing features for building classification models for ExPath.

Feature Name	**Summary Function**	**Feature Classes**
Orientation	Mean	Morphology
Orientation	Median	Morphology
Eccentricity	Skewness	Morphology
Equivalent Diameter	Skewness	Morphology
Convex Area	Kurtosis	Morphology
Minor Axis Length	Skewness	Morphology
Solidity	Kurtosis	Morphology

Solidity	Interquartile Range	Morphology
Ellipse_Minor	Interquartile Range	Morphology
Ellipse_Minor	Mean Absolute Deviation	Morphology
Ellipse_Minor	Skewness	Morphology
Minimum	Kurtosis	Intensity
Minimum	Interquartile Range	Intensity
Standard Deviation	Skewness	Intensity
Median	Kurtosis	Intensity
Mean Absolute Deviation	Skewness	Intensity
Interquartile Range	Skewness	Intensity
Interquartile Range	Kurtosis	Intensity
Kurtosis	Standard Deviation	Intensity
Kurtosis	Kurtosis	Intensity
Kurtosis	Interquartile Range	Intensity
Contrast	Interquartile Range	Texture
Contrast	Kurtosis	Texture
Contrast	Mean Absolute Deviation	Texture
Correlation	Kurtosis	Texture
Autocorrelation	Kurtosis	Texture
Autocorrelation	Skewness	Texture
Information measure Correlation 2	Kurtosis	Texture
Cluster Prominence	Mean Absolute Deviation	Texture
Dissimilarity	Skewness	Texture
Inverse Difference Moment	Interquartile Range	Texture
LRE	Skewness	Texture
GLN	Skewness	Texture
RLN	Skewness	Texture
RP	Skewness	Texture
HGRE	Kurtosis	Texture
LRHGE	Skewness	Texture
LRHGE	Mean Absolute Deviation	Texture
SRLGE	Kurtosis	Texture
SRLGE	Skewness	Texture
SRHGE	Kurtosis	Texture

Supplementary Table 11. List of top-performing features for building classification models for pre-expansion data.

Feature Name	**Summary Function**	**Feature Classes**
Ellipse	Mean	Morphology

Solidity	Mean	Morphology
Orientation	Standard Deviation	Morphology
Maximum	Standard Deviation	Intensity
Maximum	Mean	Intensity
Minimum	Standard Deviation	Intensity
Minimum	Mean	Intensity
Mean	Standard Deviation	Intensity
Standard Deviation	Standard Deviation	Intensity
Standard Deviation	Mean	Intensity
Median	Standard Deviation	Intensity
Mean Absolute Deviation	Standard Deviation	Intensity
Interquartile Range	Mean	Intensity
Skewness	Mean	Intensity
Skewness	Standard Deviation	Intensity
Kurtosis	Mean	Intensity
Kurtosis	Standard Deviation	Intensity
SRE	Mean	Texture
SRE	Standard Deviation	Texture
RLN	Mean	Texture
RP	Mean	Texture
RP	Standard Deviation	Texture
LGRE	Mean	Texture
LGRE	Standard Deviation	Texture
LRLGE	Standard Deviation	Texture
HGRE	Mean	Texture
SRLGE	Mean	Texture
SRHGE	Standard Deviation	Texture
Autocorrelation	Mean	Texture
Autocorrelation	Standard Deviation	Texture
Correlation	Standard Deviation	Texture
Correlation	Mean	Texture
Information measure Correlation 1	Mean	Texture
Information measure Correlation 2	Mean	Texture
Cluster Prominence	Standard Deviation	Texture
Cluster Prominence	Mean	Texture
Cluster Shade	Standard Deviation	Texture
Compactness	Mean	Texture
Compactness	Standard Deviation	Texture
Dissimilarity	Standard Deviation	Texture
Dissimilarity	Mean	Texture

Homogeneity	Standard Deviation	Texture
Inverse Difference Moment	Mean	Texture

Supplementary Table 12. Binary-classification results (AUC ROC; GLMNET) with or without using normalized expansion factors.

	ExPath without Normalization by the Expansion Factor	ExPath with Normalization by the Expansion Factor
Normal vs UDH	0.95	0.95
Normal vs ADH	0.96	0.96
Normal vs DCIS	0.92	0.94
UDH vs ADH	0.66	0.93
UDH vs DCIS	0.96	0.89
ADH vs DCIS	0.97	0.95

Overall, we see similar performance with or without normalization by the expansion factor, with the exception of UDH versus ADH, where the performance is significantly improved with normalization.

Supplementary Table 13. Comparison of technical capabilities of the current version of ExPath vs. electron microscopy.

	ExPath, current version	**Electron Microscopy**
Resolution	~70 nm	~0.2 nm
Multiplexity	Up to 5 colors	Only 1 color
Tissue processing time	Total: **14.5 hours** (Fresh frozen samples)	Total: **59 hours**
	Fixation: 0.3 hour	Aldehyde fixation: 1 hour
	Buffer rinse: 0.5 hour	Buffer rinse: 0.5 hours
	Heat treatment: 0.5 hour	Ethanol dehydration: 1.7 hours
	Primary antibody staining: 3 hours	Proplylene oxide treatment: 0.7 hours
	Buffer rinse: 0.5 hour	Infiltration: 30 hours
	Secondary antibody staining: 2 hours	Polymerization: 24 hours
	Buffer rinse: 0.5 hour	

	AcX incubation: 3 hours In situ polymerization: 2.5 hours Proteinase K digestion: 1 hour Buffer rinse and DAPI stain: 0.2 hours Expansion: 0.5 hours	
Tissue area that can be imaged	High	Low
Skill requirement	Low	High
Equipment requirement	Conventional microscope	Ultramicrotome and electron microscope

Supplementary Table 14. Human samples purchased from commercial sources.

Sample	**Manufacturer**	**Catalog No.**	**Figure (Main Text)**
IHC control tissue array for HER2 molecule	Abcam	ab178176	**Figures 1L** and **1M**
Human adult normal: lung (FFPE)	US Biomax	HuFPT131	**Figure 2A-J**
Multi-tumor tissue array, 95 cases of 40 types from 27 organs/sites (1.5 mm each)	Abcam	ab178234	**Figure 3**
Human adult normal: kidney (fresh frozen slides)	US Biomax	HuFTS241	**Figures 4A** and **4B.**
Breast hyperplasia tissue array, 80 cases/80 cores	US Biomax	BR806	**Figure 5**
Breast pre-cancerous disease and cancer tissue array (100 cases/101 cores)	US Biomax	BR1003	**Figure 5**
Breast common disease tissue array of 102 cases (1.5mm each)	Abcam	ab178113	**Figure 5**
Breast cancer tissue array with progressive changes, 48 cases, 96 samples (1.5mm each)	Abcam	Ab178112	**Figure 5**

Additional non-commercial whole-slide tissue sections and tissue microarrays (TMAs) prepared in our laboratories were used.

Supplementary Table 15. Primary antibodies used.

Target (reference in superscript)	**Host**	**Clonality**	**Manufacturer**	**Catalog No.**
TOM20[7]	rabbit	poly	Santa Cruz Biotech	sc-11415
Collagen IV[8]	mouse	mono	Santa Cruz Biotech	sc-59814

Vimentin[9]	chicken	poly	Abcam	ab24525
☙Tubulin[10]	rabbit	poly	Abcam	ab15246
VDAC/Porin[11]	mouse	mono	Abcam	ab14734
KRT19[12]	rabbit	poly	Sigma Aldrich	HPA002465
ACTN4[13]	rabbit	poly	Sigma Aldrich	HPA001873
Synaptopodin[14]	guinea pig	poly	PROGEN Biotechnik	GP94-IN
Actin (Smooth Muscle)[15]/ACTA2	mouse	mono	Agilent Technologies	M085129-2

Supplementary References

1. den Haan, J. M., Lehar, S. M. & Bevan, M. J. CD8(+) but not CD8(-) dendritic cells cross-prime cytotoxic T cells in vivo. *J. Exp. Med.* **192,** 1685–96 (2000).

2. den Haan, J. M. M. & Bevan, M. J. Constitutive versus activation-dependent cross-presentation of immune complexes by CD8(+) and CD8(-) dendritic cells in vivo. *J. Exp. Med.* **196,** 817–27 (2002).

3. Wu, Y. & Qu, J. Y. Autofluorescence spectroscopy of epithelial tissues. *J. Biomed. Opt.* **11,** 54023 (2006).

4. Banerjee, B., Miedema, B. E. & Chandrasekhar, H. R. Role of basement membrane collagen and elastin in the autofluorescence spectra of the colon. *J. Investig. Med.* **47,** 326–32 (1999).

5. Hansch, A. *et al.* Autofluorescence spectroscopy in whole organs with a mobile detector system. *Acad. Radiol.* **11,** 1229–1236 (2004).

6. Taha, A. A. & Hanbury, A. Metrics for evaluating 3D medical image segmentation: analysis, selection, and tool. *BMC Med. Imaging* **15,** 29 (2015).

7. Maxfield, K. E. *et al.* Comprehensive functional characterization of cancer-testis antigens defines obligate participation in multiple hallmarks of cancer. *Nat. Commun.* **6,** 8840 (2015).

8. Knutsson, J., Bagger-Sjöbäck, D. & von Unge, M. Structural tympanic membrane changes in secretory otitis media and cholesteatoma. *Otol. Neurotol.* **32,** 596–601 (2011).

9. Ware, C. B. *et al.* Derivation of naive human embryonic stem cells. *Proc. Natl. Acad. Sci. U. S. A.* **111,** 4484–9 (2014).

10. Reincke, M. *et al.* Mutations in the deubiquitinase gene USP8 cause Cushing's disease. *Nat. Genet.* **47,** 31–38 (2014).

11. Liu, T. F. *et al.* Sequential actions of SIRT1-RELB-SIRT3 coordinate nuclear-mitochondrial communication during immunometabolic adaptation to acute inflammation and sepsis. *J. Biol. Chem.* **290,** 396–408 (2015).

12. Cheng, J. *et al.* Tryptophan derivatives regulate the transcription of Oct4 in stem-like cancer cells. *Nat. Commun.* **6,** 7209 (2015).

13. Piskareva, O. *et al.* The development of cisplatin resistance in neuroblastoma is accompanied by epithelial to mesenchymal transition in vitro. *Cancer Lett.* **364,** 142–155 (2015).

14. Zhang, X. *et al.* Essential role for synaptopodin in dendritic spine plasticity of the developing hippocampus. *J. Neurosci.* **33,** 12510–8 (2013).

15. Rizeq, M. N., Van De Rijn, M., Hendrickson, M. R. & Rouse, R. V. A comparative immunohistochemical study of uterine smooth muscle neoplasms with emphasis on the epithelioid variant. *Hum. Pathol.* **25,** 671–677 (1994).